

Corrosivity and Thermal Stability of Biocrude Oil for Co-Processing in FCC Feedlines: An  
Investigation and Risk Assessment

by

Henry Brian Pedraza

A thesis submitted in partial fulfillment of the requirements for the degree of

Master of Science

in

Materials Engineering

Department of Chemical and Materials Engineering  
University of Alberta

© Henry Brian Pedraza, 2023

# ABSTRACT

Fast pyrolysis bio-oil is a promising renewable energy source derived from biomass. However, its high corrosivity and poor thermal stability have limited its widespread use as a drop-in fuel. One promising method for transforming low-quality biocrudes into drop-in fuels is co-processing with petroleum intermediates in existing fluid catalytic cracking (FCC) units. Co-processing BO with petroleum intermediates in FCC units requires careful consideration of the corrosion resistance from the feed injection system and the BO thermal stability, particularly since feedstocks are usually preheated to 100–300 °C before injection. In this study, we investigated the corrosion resistance of several structural materials commonly used in FCC units, including carbon steel (CS), chromoly steel (P91), stainless steels (SS) 304L and 316L, and a nickel-based alloy (HX), and the aging risk of BO at a temperature range of 80–220 °C. Our results showed that CS performed poorly at each testing temperature, exhibiting severe corrosion. In contrast, P91 showed a lower corrosion rate of 3.497 mm/y at 80 °C for 24 hours, but its corrosion rate increased as the temperature increased. In the immersion experiment at 220 °C, the corrosion rate of P91 surpassed that of CS, reaching a value of 73.32 mm/y. SS 304L and 316L exhibited an acceptable corrosion rate of 0.29 mm/y and 0.06 mm/y at 80 °C, but their corrosion rate increased dramatically as the temperature increased. HX was not affected at any of the studied temperatures. As to the thermal stability, we observed the occurrence of phase separation, with BO separating into liquid and solid phases at all three temperatures. As the temperature increased, we noticed a significant change in the physicochemical properties of the phases. Furthermore, one critical finding from our study was the identification of a temperature threshold of 80 °C. At this temperature, we observed both active corrosion of steels in BO and fast aging of the BO.

# PREFACE

This thesis is an original work by Henry Pedraza. I was responsible for data collection and the setup and writing of the manuscript under the supervision and edition of Dr. Jing Liu. Part of the Chapter 3, Chapter 4, and Chapter 5 have been published and presented as *H. Pedraza, H. Wang, X. Han, Y. Zeng and J. Liu, "Investigating the thermal stability and corrosivity of biocrude oil at FCC feeding temperatures for co-processing applications" AMPP 2023* and *H. Pedraza, H. Wang, X. Han, Y. Zeng and J. Liu, "Corrosion and Aging Risk Assessment of the co-FCC Feed Injection System" Biomass and Bioenergy 2023*.

# DEDICATION

*To the most important people in my life, who have supported me through every step of this journey. To my wife Anastasiia, thank you for your unwavering love, encouragement, and understanding. To my parents, Henry and Maria, thank you for always believing in me and for instilling in me passion for learning and strong work ethic. To my sisters Angie and Caroll and their families, thank you for your support and encouragement. To my wife's family, thank you for welcoming me into your family with open arms and for your support. I dedicate this thesis to all of you with all my heart.*

# ACKNOWLEDGEMENTS

First and foremost, I am indebted to my supervisor, Dr. Jing Liu, whose exceptional dedication and patience have been instrumental in shaping my research skills. Her unwavering support, guidance, and inspiration have been invaluable to me and have helped me to become a better researcher.

Also, I would like to extend a special note of thanks to Haoxiang Wang, my lab mate, whose guidance and mentorship have been instrumental in helping me improve my research skills. Furthermore, I am also grateful to the rest of the team, Dr. Meifeng Li, Haofei Sun, Idil Mutlu, Ben Taylor, Emily Seto, Ula Suliman, Farhan Khalid, and Alexander Gross, who have made my time in the lab enjoyable and memorable. Their insights, expertise, and friendship have been essential in helping me to navigate the challenges of research.

I would also like to extend my thanks to Daniela Arango and Ezz Ahmed, former members of Dr. Liu's group, for their guidance and support during my early days in the lab. Finally, I would like to acknowledge the financial support I received for this study from the Canadian NRCan OERD Clean Energy Program and Forest Innovation Program, as well as from the Natural Science and Engineering Research Council of Canada (NSERC).

Thank you all for your invaluable contributions to my academic journey.

# TABLE OF CONTENTS

ABSTRACT.....	ii
PREFACE .....	iii
DEDICATION.....	iv
ACKNOWLEDGEMENTS.....	v
TABLE OF CONTENTS.....	vi
LIST OF TABLES .....	ix
LIST OF FIGURES .....	xi
LIST OF ABBREVIATIONS .....	xv
LIST OF SYMBOLS.....	xvii
CHAPTER 1 INTRODUCTION .....	1
1. 1 BACKGROUND OF BIO-OIL PRODUCTION.....	1
1. 2 PYROLYSIS OIL AND ITS PROPERTIES .....	2
1. 3 GENERAL CHALLENGES IN CO-PROCESSING PYROLYSIS OIL .....	4
1. 4 RESEARCH OBJECTIVES .....	8
1. 5 THESIS OUTLINE .....	9
CHAPTER 2 CORROSION CHALLENGES IN HANDLING PYROLYSIS OIL .....	10
2. 1 CORROSION IN PYROLYSIS OIL .....	10

2. 2 CORROSION IN BO AND ITS BLENDS WITH PETROLEUM FRACTIONS .....	16
2. 3 CORROSION IN MODEL BOs .....	19
2. 4 CORROSION IN BO AND ITS BLENDS WITH ADDITIVES .....	24
2. 5 SUMMARY OF CORROSION CHALLENGES.....	29
CHAPTER 3 EXPERIMENTAL PROCEDURES .....	31
3. 1 PREPARATION OF METAL COUPONS.....	31
3. 2 IMMERSION EXPERIMENTS SET-UP .....	32
3. 3 IMMersed SAMPLES POST-CHARACTERIZATION .....	37
3. 4 AGING EXPERIMENTS SET-UP .....	41
CHAPTER 4 CORROSION OF STEELS IN PYROLYSIS OIL UP TO 220 °C .....	43
4. 1 CARBON STEEL (CS) A36 IN BO .....	44
4. 2 CHROMOLY STEEL P91 IN BO .....	52
4. 3 STAINLESS STEEL 304L IN BO .....	57
4. 4 STAINLESS STEEL 316L IN BO .....	60
4. 5 NICKEL-BASED ALLOY HX IN BO.....	67
CHAPTER 5 THERMOSTABILITY OF PYROLYSIS OIL UP TO 220 °C.....	72
5. 1 AGING EXPERIMENTS OF BO AT 80 °C .....	72
5. 2 AGING EXPERIMENTS OF BO AT 150 °C .....	76
5. 3 AGING EXPERIMENTS OF BO AT 220 °C .....	80

5. 4 SUMMARY OF INFLUENCE OF AGING TEMPERATURE ON PHASE SEPARATION .....	82
5. 5 SOLID CONTENT IN AGING EXPERIMENTS .....	85
5. 6 INFLUENCE OF METALLIC SPECIES IN BO AGING .....	86
CHAPTER 6 CONCLUSIONS AND FUTURE WORK .....	89
6. 1 CONCLUSIONS .....	89
6. 2 FUTURE WORK .....	91
REFERENCES .....	92
APPENDIX A – CHEMICAL COMPOSITIONS .....	103
A.1 CHEMICAL COMPOSITIONS OF STRUCTURAL STEELS .....	103

# LIST OF TABLES

<b>Table 1. 1.</b> Primary features of BO originated from biomass. ....	<b>4</b>
<b>Table 2. 1.</b> Previous results of immersion test in a BO environment. ....	<b>12</b>
<b>Table 2. 2.</b> Previous results of EC tests in a BO environment. ....	<b>15</b>
<b>Table 2. 3.</b> Previous results of immersion test in BO/fossil fuel intermediates blends. ....	<b>18</b>
<b>Table 2. 4.</b> Previous results of immersion test in model BOs environments. ....	<b>21</b>
<b>Table 2. 5.</b> Previous results of immersion test in a BO with corrosion inhibitors environment. .	<b>27</b>
<b>Table 3. 1.</b> Chemical compositions (wt.%) of selected structural metals. ....	<b>32</b>
<b>Table 3. 2.</b> Properties of BO used in immersion and aging experiments. ....	<b>36</b>
<b>Table 4. 1.</b> Categorization of corrosion rates in oil production systems, NACE–SP0775-2018 and Bradford et al. (2001) [53], [54]. ....	<b>46</b>
<b>Table 4. 2.</b> Pressure registered in immersion experiments with different sets of immersed metal coupons in BO for 10 and 24 hours at 80 to 220 °C. ....	<b>50</b>
<b>Table 4. 3.</b> Pressure registered in immersion experiments when 0.5 g of Fe <sub>2</sub> O <sub>3</sub> were added to BO for 10 hours at 150 and 220 °C. ....	<b>51</b>
<b>Table 5. 1.</b> Phase separation in aging experiments at 80 °C for 24, 96, and 168 hours. (a) film; (b) top+ bottom (liquid phase). ....	<b>73</b>
<b>Table 5. 2.</b> Phase separation in aging experiments at 150 °C for 24, 96, and 168 hours. (a) film; (b) top layer (liquid phase); and (c) bottom layer (solid phase). ....	<b>77</b>
<b>Table 5. 3.</b> Phase separation in aging experiments at 220 °C for 24, 96, and 168 hours. (a) film; (b) top layer (liquid phase); and (c) bottom layer (solid phase). ....	<b>80</b>

**Table 5. 4.** Summary of phase separation from aging experiments at 80, 150 and 220 °C for 24, 96, and 168 hours..... **84**

**Table A.1. 1.** Chemical compositions of commonly used structural steels in co-processing applications testes in previous studies. .... **104**

# LIST OF FIGURES

<b>Figure 1. 1.</b> Van Krevelen diagram. First generation biofuels (■), second generation biofuels (●), third generation biofuels (▲), and intermediate fossil fuels (◆). Adapted from [24].....	5
<b>Figure 2. 1.</b> Randle circuit utilized for fitting impedance data in the majority of EIS experiments. Adapted from [27].....	14
<b>Figure 3. 1.</b> The apparatus used for immersion and aging experiments. (a) front view; (b) left view; (c) right view; and (d) metal coupons anchored to PTFE holder before immersion. ....	34
<b>Figure 3. 2.</b> Optical micrographs of etched metals used in immersion experiments. (a) CS; (b) SS 304L; and (c) SS 316L. Microstructures of commonly used P91 [49] and HX [53] can be found in the reference.....	39
<b>Figure 3. 3.</b> Schematic of phase separation in BO aging experiments at 150 °C. ....	41
<b>Figure 4. 1.</b> Photographic images of CS: (a) before immersion; after immersion for 24 hours in BO (b) at 80 °C, (c) 150 °C, (d) and 220 °C.....	45
<b>Figure 4. 2.</b> The averaged corrosion rates of CS after 10 and 24 hours of immersion in BO at 80 to 220 °C. ....	46
<b>Figure 4. 3.</b> Dependence of the corrosion rate of CS on the temperature (80–220 °C) according to the Arrhenius plot for BO, (a) logarithm of the Arrhenius equation, and (b) the Arrhenius equation. ....	47
<b>Figure 4. 4.</b> Morphology of CS after 24 hours of immersion in BO. (a) at 80 °C; (b) at 150 °C; and (c) at 220 °C.....	48
<b>Figure 4. 5.</b> Photographic images of CS: (a) before immersion; after immersion for 10 hours in BO (b) at 80 °C, (c) 150 °C, (d) and 220 °C.....	49

<b>Figure 4. 6.</b> Photographic images of P91: (a) before immersion; after immersion for 24 hours in BO (b) at 80 °C, (c) 150 °C, (d) and 220 °C.....	<b>52</b>
<b>Figure 4. 7.</b> The averaged corrosion rates of P91 after 10 and 24 hours of immersion in BO at 80 to 220 °C compared to those of CS.....	<b>53</b>
<b>Figure 4. 8.</b> Dependence of the corrosion rate of P91 on the temperature (80–220 °C) according to the Arrhenius plot for BO, (a) logarithm of the Arrhenius equation, and (b) the Arrhenius equation.....	<b>54</b>
<b>Figure 4. 9.</b> Morphology of P91 after 24 hours of immersion in BO. (a) at 80 °C; (b) at 150 °C; and (c) at 220 °C. ....	<b>55</b>
<b>Figure 4. 10.</b> Photographic images of P91: (a) before immersion; after immersion for 10 hours in BO (b) at 80 °C, (c) 150 °C, (d) and 220 °C.....	<b>56</b>
<b>Figure 4. 11.</b> Photographic images of SS 304L: (a) before immersion; after immersion for 24 hours in BO (b) at 80 °C, (c) 150 °C, (d) and 220 °C.....	<b>57</b>
<b>Figure 4. 12.</b> Dependence of the corrosion rate of SS 304L on the temperature (80–220 °C) according to the Arrhenius plot for BO, (a) logarithm of the Arrhenius equation, and (b) the Arrhenius equation.....	<b>58</b>
<b>Figure 4. 13.</b> Morphology of SS 304L after 24 hours of immersion in BO. (a) at 80 °C; (b) at 150 °C; and (c) at 220 °C.....	<b>60</b>
<b>Figure 4. 14.</b> Photographic images of SS 316L: (a) before immersion; after immersion in BO (b) at 80 °C, (c) 150 °C, (d) and 220 °C. ....	<b>61</b>
<b>Figure 4. 15.</b> XRD patterns recorded on post-immersion SS 316L coupons.....	<b>62</b>
<b>Figure 4. 16.</b> SEM images and EDS maps from a cross-section of SS 316L. (a) at 80 °C; and (b) at 150 °C. ....	<b>63</b>

<b>Figure 4. 17.</b> SEM images and its corresponding compositional mapping by EDS from a cross-section of SS 316L at 220 °C.....	<b>63</b>
<b>Figure 4. 18.</b> Effect of temperature on the corrosion rate of SS 316L compared to commonly used structural SS 304L.....	<b>65</b>
<b>Figure 4. 19.</b> Dependence of the corrosion rate of SS 316L on the temperature (80–220 °C) according to the Arrhenius plot for BO, (a) logarithm of the Arrhenius equation, and (b) the Arrhenius equation.....	<b>66</b>
<b>Figure 4. 20.</b> Morphology of SS 316L after 24 hours of immersion in BO. (a) at 80 °C; (b) at 150 °C; and (c) at 220 °C.....	<b>67</b>
<b>Figure 4. 21.</b> Photographic images of HX: (a) before immersion; after immersion in BO (b) at 80 °C, (c) 150 °C, (d) and 220 °C.....	<b>68</b>
<b>Figure 4. 22.</b> The averaged corrosion rates of the five metals studied after 24 hours of immersion in BO at 80 to 220 °C.....	<b>69</b>
<b>Figure 4. 23.</b> SEM micrographs of the cross-sections of corroded samples at 150 °C. (a) CS; (b) P91; (c) SS 304L; (d) SS 316L; and (e) HX. ....	<b>69</b>
<b>Figure 4. 24.</b> Dependence of the corrosion rate of HX on the temperature (80–220 °C) according to the Arrhenius plot for BO, (a) logarithm of the Arrhenius equation, and (b) the Arrhenius equation.....	<b>70</b>
<b>Figure 4. 25.</b> Morphology of HX after 24 hours of immersion in BO. (a) at 80 °C; (b) at 150 °C; and (c) at 220 °C. ....	<b>71</b>
<b>Figure 5. 1.</b> TG and DTG curve of BO/Stock.....	<b>74</b>
<b>Figure 5. 2.</b> Influence of aging time in the TG curves of phase separation at 80 °C.....	<b>75</b>
<b>Figure 5. 3.</b> Schematic of phase separation in BO aging experiments at 80 °C.....	<b>75</b>

<b>Figure 5. 4.</b> Schematic of phase separation in BO aging experiments at 150 °C. ....	<b>78</b>
<b>Figure 5. 5.</b> Influence of aging time in the TG curves of phase separation at 150 °C. ....	<b>79</b>
<b>Figure 5. 6.</b> Schematic of phase separation in BO aging experiments at 220 °C. ....	<b>82</b>
<b>Figure 5. 7.</b> Influence of aging time in the TG curves of phase separation at 220 °C. ....	<b>82</b>
<b>Figure 5. 8.</b> Influence of temperature in phase separation. (a) TG curves in aging experiments for 24 hours, and (b) TG curves in aging experiments for 96 hours. ....	<b>83</b>
<b>Figure 5. 9.</b> Influence of temperature in solid content production in aging experiments. ....	<b>86</b>
<b>Figure 5. 10.</b> Influence of immersed metal (CS) in BO aging. ....	<b>87</b>
<b>Figure 5. 11.</b> Influence of immersed Fe-oxide in BO aging. ....	<b>87</b>

# LIST OF ABBREVIATIONS

BO:	Bio-oil
CS:	Carbon steel
DI:	Deionized water
DTG:	Derivative of thermogravimetric curve
EC:	Electrochemical
EDS:	Energy dispersive spectroscopy
EIS:	Electrochemical impedance spectroscopy
FCC:	Fluid catalytic cracking
FP:	Fast pyrolysis
FPO:	Fast pyrolysis oil
GC/MS:	Gas chromatography/mass spectrometry
HDO:	Hydrodeoxygenated
HFO:	Heavy fuel oil
HTL:	Hydrothermal liquefaction
HX:	Hastelloy-X
LHV:	Low heating value
MOC:	Materials of construction
OM:	Optical microscopy
RT:	Room temperature
SE:	Secondary electrons

SEM: Scanning electron microscopy  
SS: Stainless steel  
TAN: Total acid number  
TGA: Thermogravimetric analysis  
UCO: Used cooking oil  
VGO: Vacuum gas oil  
XRD: X-ray diffraction

# LIST OF SYMBOLS

Symbol	Description	Units
A	Arrhenius constant	-
Ar	Area of the coupon	cm <sup>2</sup>
D	Density	g/cm <sup>3</sup>
H <sup>+</sup>	Hydrogen ions	-
K	Constant (87600)	mm/y.cm
R	Universal gas constant	J/molK
R <sub>2</sub>	Resistance against charge transfer	ohm.cm <sup>2</sup>
t	Time of exposure	h
T	Temperature	K
t <sub>cr</sub>	Critical time	h
T <sub>cr</sub>	Critical temperature	°C
W	Weight loss	g
ΔE	Molar activation energy	KJ/mol

# CHAPTER 1 INTRODUCTION

## 1. 1 BACKGROUND OF BIO-OIL PRODUCTION

Governments worldwide are focused on minimizing the environmental impact of traditional fossil fuel combustion [1]. The industrial combustion of fossil fuels contributes to approximately 98% of the total carbon emissions across the globe. Thus, a decrease in the use of fossil fuels is crucial to restraining greenhouse gas emissions [2], [3]. Attempts to minimize these impacts may come from different sources but the production of green energy has emerged as a solution to this problem. The focus has shifted toward developing emission-free fuels [4]. For example, biomass, a renewable energy source, can be converted into bio-oil (BO) through fast/flash pyrolysis (FP) and hydrothermal liquefaction (HTL) [5], [6]. Biomass sources include wood, forest residues, organic waste, agricultural waste, and aquatic plants [5], [6]. BO has several advantages over traditional fossil fuels. For instance, biofuels are the most available carbon-neutral fuel, as the CO<sub>2</sub> generated during combustion is the same amount absorbed by the source of biomass during its growth [7]. Additionally, BO combustion produces lower SO<sub>x</sub> and NO<sub>x</sub> emissions compared to regular fossil fuels, and it provides a solution for the waste management of agricultural and forestry residues [6], [8].

HTL, as a conversion process, has a few advantages over FP. HTL does not require drying of biomass, as water serves as a solvent in the process, which allows for lower temperatures (280–370 °C) and heating rates. Furthermore, HTL provides a solution for the management of wet waste biomass in densely populated locations [6]. However, HTL is still not a mature technology and

requires further development before its widespread use [9]. On the other hand, FP is currently the only commercially viable thermochemical technology for producing large amounts of BO. In this process, the biomass is rapidly heated without oxygen or with less oxygen than required for complete combustion [5]. The following section will explore the properties and limitations of BO or fast pyrolysis oil (FPO) produced through FP.

## **1. 2 PYROLYSIS OIL AND ITS PROPERTIES**

Biomass is composed of oxygenated organic polymers, primarily cellulose (40–60 wt.%), hemicellulose (20–40 wt.%), and lignin (10–25 wt.%) [5], [10], [11]. These three main components undergo thermal decomposition in a specific pattern in FP process. Moisture evolves from room temperature (RT) to 220 °C, hemicellulose decomposes between 220–315 °C, cellulose decomposes between 315–400 °C, and lignin decomposes at temperatures above 400 °C [11].

The decomposition of biomass results in BO with a dark brown appearance and a complex mixture of constituents with a wide range of molecular sizes. The chemical composition of BO is very complicated, and some compounds are not detectable. Approximately just 30 wt.% of BO can be detected by gas chromatography/mass spectrometry (GC/MS) [12]. Hence, BO composition is broadly described as a mixture of water (19–30 wt.%), detectable organic compounds (20–30 wt.%), and oligomers (water-soluble and water-insoluble) (43–59 wt.%). The water-insoluble oligomers are lignin-derived products with high carbon content [12]. BO contains 45–50 wt.% of oxygen due to the severe presence of oxygenated compounds, as its predecessor biomass, which are approximately 300 within BO, such as hydroxyaldehydes, hydroxyketones, sugars, carboxylic acids, and phenols [5], [12]. Also, part of the oxygen content is supplied by the high-water content

( $\approx$  25 wt.%) in BO [3], [5]. The water content in BO leads to a poor low heating value (LHV), which is nearly 40% of the fossil fuels LHV. The LHV or net calorific value accounts for the heat the fuel produces when goes through a complete combustion [13].

The organic compounds found in BO include acids, alcohols, aldehydes, esters, ketones, phenols, syringols, sugars, furans, alkenes, aromatics, nitrogen compounds, and miscellaneous oxygenates [5]. These compounds contribute to a total acid number (TAN) of nearly 70, which explains a low pH of BO between 2 and 3 [5], [14]. Consequently, BO is steered to another unwanted property, high corrosiveness [15]. These organic compounds within BO have reactive functional groups such as hydroxyl, carbonyl, and carboxyl. They interact with each other through different reactions, such as etherification, acetalization, and polymerization [3], [16]. Consequently, compounds with higher molecular weight are formed, leading to an increment in viscosity [3]. This change in physical properties with time due to BO instability is also known as aging [17]. Many research studies have been initiated to address the aging/instability issue of BO. Elliott et al. [18] evaluated the BO instability in 45 mL samples heated at 80 °C for 24 hours, with a cooling down of 1.5 hours. After aging experiments, they observed that the initial viscosity (30.4 cSt) experienced an 88% increment (57.3 cSt). Besides this, another sample with an initial viscosity of 26.7 cSt suffered phase separation, preventing the authors from determining the final viscosity [18].

When phase separation occurs in BO during aging experiments, the BO instability can be addressed through thermoanalysis technologies [16]. For example, Chaala et al. [19] conducted aging experiments in BO at 80 °C for 168 hours. They implemented thermogravimetric analysis

(TGA) to assess the thermal susceptibility of different layers in BO. Two different fractions (upper and bottom layers) were collected from the BO sample. By comparing the TG curves of the initial BO and upper layer, they observed that the former curve shifted upper right, obtaining a 36 °C increment in the weight loss. They attributed this behavior to the compounds within initial BO polymerizing without forming lower molecular weight components [19]. In a word, BO, which inherits its features (**Table 1. 1**) from biomass, poses three major challenges for traditional refining operations: high corrosiveness, high thermal instability, and immiscibility with petroleum intermediates.

**Table 1. 1.** Primary features of BO originated from biomass.

<b>Property</b>	<b>Value</b>	<b>Ref (s)</b>
Oxygen content	45–50 wt.%	[5], [12]
Water content	19–30 wt.%	[12]
TAN	~ 70 mgKOH/g	[14]
pH value	2–3	[5]
Heating Value	40 % of fossil fuels' LHV	[13]

### **1. 3 GENERAL CHALLENGES IN CO-PROCESSING PYROLYSIS OIL**

The use of BO as a drop-in fuel is challenged by its undesired properties, as highlighted above. Pinho et al. [20] suggested that BO should be treated as an intermediate product in the thermochemical biomass pathway and upgraded to produce transportation fuels [20]. Upgrades in BO mainly involve deoxygenating the highly-oxygenated molecules, aforementioned [12]. Several authors have proposed different routes to upgrade BO, for instance, the molecules in BO can be deoxygenated, cracked, or hydrogenated [12].

One may believe that BO can be processed in the fluid catalytic cracking (FCC) unit like traditional fossil fuels. However, previous authors have found that direct injection of BO in the FCC unit is unreasonable due to the unwished amount of char and coke sub-production [20]. Alternatively, BO can be deoxygenated through hydroprocessing, which involves the presence of hydrogen, but this process is expensive and complex due to the different factors that should be considered, such as hydrogen source, temperature, pressure, and type of catalyst [12], [21]. Hence, the costs of establishing and operating a bio-refinery for hydrodeoxygenated BO (HDO-BO) processing are incredibly high [22]. Besides, HDO-BO still requires upgrading operation units such as fractionation, cracking, and isomerization [8]. For instance, Fogassy et al. [23] saw the potential to co-process HDO-BO with vacuum gas oil (VGO) in the FCC units, as they have a similar hydrogen-to-carbon ratio, as shown in **Figure 1. 1**. They found comparable gasoline yields when they co-processed 80 wt.% VGO and 20 wt.% HDO-BO, as compared to 100 wt.% VGO cracking. However, the product composition was enriched in coke, olefins, and aromatics [23].

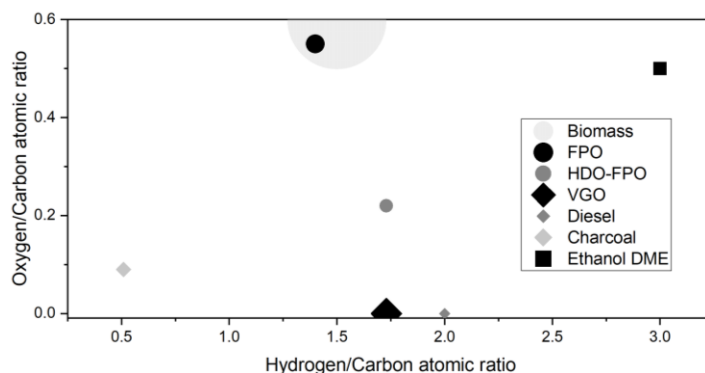


**Figure 1. 1.** Van Krevelen diagram. First generation biofuels (■), second generation biofuels (●), third generation biofuels (▲), and intermediate fossil fuels (◆). Adapted from [23].

Furthermore, existing FCC units are still considered a route to upgrade BO as a co-processing feedstock. By performing this co-processing, the capital and operational costs can be reduced up to 20% compared to pure BO catalytic cracking. As a result, the production cost of biofuel will be reduced, making co-processing a more feasible option compared to building a new bio-refinery from scratch [8], [22]. BO properties will be upgraded due to the hydrogen-enriched petroleum hydrocarbons, such as VGO, can transfer hydrogen to BO by reacting with their molecules rich in oxygen [8]. FCC as a co-process unit is economically attractive since external hydrogen injection is not required, and the catalysts can be regenerated in situ [21].

Yet, co-processing raises some challenges, as well. For example, BO is practically immiscible with VGO due to its high oxygen content and, thus, polarity. In addition, BO is thermally unstable and undergoes extensive unwanted polymerization at relatively low temperatures (50 °C) [16], [20]. Pinho et al. [20] elegantly solved this issue by providing two separate feeding lines for VGO and BO. In this way, they could heat up the two liquids at two different temperatures, avoiding extensive coking. VGO was injected at a temperature range of 220–280 °C, whereas BO was injected through a nozzle below the injection point for VGO at a temperature lower than 50 °C. The co-processing was performed in a 10–20 % BO and 90–80 % VGO feed charge at 540–560 °C for two hours. The authors observed a yield similar to treating 100% VGO when the BO was 10% of the feed charge. The biocrude and petroleum crudes are not mixed or emulsified prior to co-processing. Therefore, the possibility to preheat VGO at a temperature higher than 200 °C lowers its viscosity and improves the dispersion of BO itself. Hydrocarbon feedstocks are preheated in the traditional FCC process at 100–300 °C [20], [24].

Unfortunately, co-processing BO is limited because its instability and corrosivity at temperatures above 50 °C are not fully addressed and understood. If the limitations are not addressed, the following problems may arise during co-processing. An increment in BO viscosity due to instability leads to flow conveying issues, e.g., the pipelines in refineries will present high-pressure drops requiring more costly equipment and higher pumping costs. In addition, this instability promotes layer generation creating extra filtration problems [5]. Besides this, the high corrosiveness of BO is not acceptable for the metals commonly used in a crude refinery, such as low-alloy steels (microalloyed, chromoly, and carbon steel (CS)), which represent 80% of metals used in refining operations, along with various grades of stainless steels (SSs) [25].

## 1. 4 RESEARCH OBJECTIVES

The aim of this work is to investigate the corrosivity and thermal stability of BO at Fluid Catalytic Cracking (FCC) feeding temperatures of 100–300 °C. A series of experiments have been designed and performed to achieve the following objectives:

- To study the effect of temperature and alloying elements on BO corrosivity. Immersion experiments are performed at different temperatures and times in five structural steels containing different alloying elements. Optical microscopy (OM) and scanning electron microscopy (SEM) micrographs are taken after corrosion. The corrosion rates and chemical compositions of the steels are analyzed to generate trends.
- To identify the effect of temperature on BO stability. Aging experiments are performed to assess the BO stability as temperature and storage time increases. Changes in the physical properties of BO, such as viscosity, density, and pH, are recorded in aged samples. TGA is carried out in aged samples to corroborate changes.
- To propose the influence of BO instability on BO corrosivity and vice-versa. Correlation of the dataset from objective 1 and objective 2 to establish any connections. Overall, this study aims to improve our understanding of the behavior of BO in FCC units and provide insight into its corrosivity and thermal stability. Based on the results, further work needed will be determined.

## 1. 5 THESIS OUTLINE

**Chapter 1** presents the research background, motivations, and objectives to be accomplished.

**Chapter 2** reviews existing methodologies, progress, and knowledge gaps in the research on corrosion challenges during BO storage and co-processing. This chapter focuses on BO, BO blends, and model BOs.

**Chapter 3** presents detailed experimental procedures for immersion experiments with 5 structural metals (such as carbon steel, chromoly steel, stainless steels, and a nickel-based alloy) in BO, as well as parallel aging experiments of BO at co-processing temperatures. This chapter also covers methods for characterizing the metals and BO.

**Chapter 4** focuses on the corrosivity of BO at 80, 150 and 220 °C. Long-term immersion experiments were performed for up to 24 hours to investigate the corrosion with 5 structural metals in BO. Post-experimental characterization was applied to explain the corrosion mechanism.

**Chapter 5** examines the thermal stability of BO at 80, 150 and 220 °C. BO samples (i.e., without metals immersed in) were aged for various time periods at each temperature, and phase separation (liquid and solid phase) of BO was observed due to aging. BO samples were further investigated via thermoanalysis, and changes in physical and chemical properties were recorded. This chapter also correlates with the results of Chapters 4 and 5.

**Chapter 6** summarizes experimental findings and delivers recommendations for future research.

# CHAPTER 2 CORROSION CHALLENGES IN HANDLING PYROLYSIS OIL

As aforementioned, BO has a low pH (2–3) due to high acid content such as hydroxy acetaldehyde ( $\geq 10$  wt.%), acetic acid ( $\approx 5$  wt.%), and formic acid ( $\approx 3$  wt.%) resulting in higher corrosivity compared to fossil fuels [5], [26]. The materials of construction (MOCs) in the FCC unit, which is the heart of crude refineries, are the same as those commonly used throughout the entire refining operation (microalloyed, chromoly, CSs, and SSs) [25]. For instance, SS 304L and CS are widely used in different components along the FCC flowsheet; SS 304L is used in the nozzles in the feed injection and air distributor systems as well as the regenerator cyclone, while CS is used in the riser, spent catalyst stripper, feeding pipes, and standpipe system [27]. The purpose of this chapter is to review existing methodologies, progress, and knowledge gaps in research related to the corrosion challenges associated with BO handling.

## 2.1 CORROSION IN PYROLYSIS OIL

There have been a few studies examining the corrosivity of BO on these structural steels through immersion experiments, as summarized in **Table 2.1**. Keiser et al. [28] carried out immersion experiments on BOs derived from two different sources of biomass (red oak and corn stover). They found high acidity or high total acid number (TAN) in the different fractions of BO, due to high concentrations of formic and acetic acid [28]. They tested different grades of structural steels and found a corrosion rate of 2.96 and 3.41 mm/y for CS in red oak-derived and corn stover-derived BO, respectively. The 2.25Cr-1Mo steel presented a corrosion rate of 2.45 mm/y in the

red oak-derived BO and 4.97 mm/y in the corn stover-derived BO. The authors linked the higher corrosion rates to higher TAN in the BO. The 300 series SS (304L and 316L) showed negligible corrosion in both BOs. However, localized attack through the grain boundaries, or intergranular corrosion, was observed during post-characterization. The results on SS 409 varied greatly, with a corrosion rate of 0.44 mm/y in red oak-derived BO and 3.00 mm/y in corn stover-derived BO. The authors attributed the discrepancy in corrosion results for coupons from the same steel to the acidity of the fraction where the coupons were immersed, with the fractions used from corn stover-derived BO being more aggressive than those from red oak [28].

Keiser et al. [29] also conducted immersion experiments with BO derived from pine whitewood and pine residues, which were low and high ash biomass sources, respectively. They varied the ash and moisture content of the BOs (designated as H for high, L for low, A for ash, and M for moisture) and performed immersion tests at 50 °C for 500 and 1000 hours. The goal was to determine the influence of the alloying element (Cr) on corrosion resistance in a BO environment, using plain steel (CS), low-alloy steel (chromoly steel), and high-alloy steel (SS). They determined a corrosion rate of up to 2 mm/year for CS (1018), while chromoly steel 2.25Cr-1Mo had a corrosion rate of approximately 3 mm/y. SS 304L and SS 316L exhibited less than 0.01 mm/year at 50 °C for 500 and 1000 hours. After 1000 hours of immersion, SS 409 showed approximately 3 mm/y in the different BOs, with the highest corrosion susceptibility under LALM BO. On the other hand, SS 409 exhibited less than 1 mm/y when the immersion experiment was up to 500 hours [29]. As expected, the corrosion resistance worsened with increasing immersion time. The authors also observed a slight dependence of high ash content on a high TAN in the different BOs.

Wang et al. [3] conducted immersion tests on pinewood-derived BO at 50 and 80 °C for 168 hours. They determined a corrosion rate for CS (A36) of 1.5 and 7.2 mm/y at 50 and 80 °C, respectively. No corrosion was observed at 50 °C in SS 304L and SS 316L, whereas at 80 °C, it exhibited 0.8 and less than 0.1 mm/y for SS 304L and SS 316L, respectively [3]. They observed that steels with higher additions of molybdenum (Mo) and nickel (Ni) are less susceptible to be corroded under BO constituents and therefore the highest corrosion resistance was observed in SS 316L, which comprises higher Mo and Ni concentrations in its chemical composition [3].

**Table 2. 1.** Previous results of immersion test in a BO environment.

<b>Alloy</b>	<b>Environment</b>	<b>Temperature (°C)</b>	<b>Time (h)</b>	<b>Corrosion rate (mm/y)</b>	<b>Ref (s)</b>
A36 CS	Pine BO	50	168	1.5	[3]
	Pine BO	80		7.2	
1018 CS	Corn Stover BO	50	500	3.41	[28]
	Red Oak BO			2.96	
	LALM BO			2.50	
	HALM BO			1.30	
	HAHM BO		1000	1.69	[29]
	HAHM BO			1.57	
	LALM BO			2.08	
	Corn Stover BO			4.97	
2.25Cr-1Mo	Red Oak BO	50	500	2.45	[28]
	LALM BO			3.29	
	HALM BO			2.23	
	HAHM BO		1000	2.83	[29]
	HAHM BO			2.64	
	LALM BO			2.92	
	LALM BO			2.92	

SS 304L	Pine BO	50	168	None	[3]
	Pine BO	80		0.8	
	Corn Stover BO		500	<0.01	[28]
	Red Oak BO			<0.01	
	HAHM BO	50		<0.01	
	LALM BO		1000	<0.01	[29]
	HALM BO			<0.01	
	HAHM BO			<0.01	
	LALM BO			<0.01	
SS 316L	Pine BO	50	168	None	[3]
	Pine BO	80		<0.1	
	LALM BO		1000	<0.01	[29]
	HALM BO			<0.01	
	HAHM BO	50		<0.01	
	LALM BO		500	<0.01	[28]
	HAHM BO			<0.01	
	Corn Stover BO			<0.01	
	Red Oak BO			<0.01	
SS 409	Corn Stover BO		500	3.00	[28]
	Red Oak BO			0.44	
	HAHM BO			0.94	
	LALM BO	50	1000	3.29	[29]
	HALM BO			2.23	
	HAHM BO			2.64	
LALM BO			2.92		

*Note: H, L, A, M stand for high, low, ash, and moisture, respectively. The metal compositions can be found in Appendix A.*

On parallel, other authors have assessed the corrosion susceptibility of structural metals by performing electrochemical (EC) experiments. The most used EC test is electrochemical impedance spectroscopy (EIS), which provides a quick way to determine the corrosion behavior of alloys compared to immersion experiments. The results of EIS tests are usually represented in Nyquist plots, which plot the real impedance ( $Z'$ ) against the imaginary impedance ( $Z''$ ) [30]. The corrosion susceptibility of a metal can be roughly determined by calculating the difference between the highest and lowest  $Z'$  values on a Nyquist plot [10], [26]. The corrosion resistance of the metal against BO constituents is indicated by the fitted  $R_2$  in a Randle circuit, as depicted in **Figure 2. 1** [26]. This fitted  $R_2$  is a quantitative measurement of the global resistance against charge transfer when a passive film is formed. Hence, a low  $R_2$  is strongly related to higher corrosion susceptibility in that environment, due to the passive film is not stable to limit the charge transfer process [10].

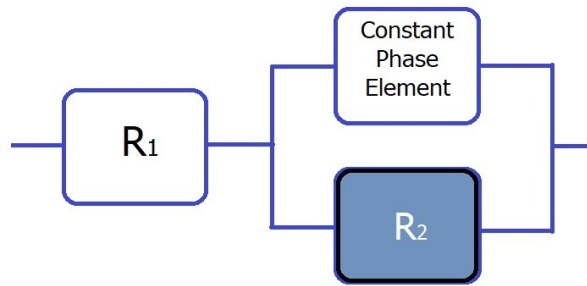


**Figure 2. 1.** Randle circuit utilized for fitting impedance data in the majority of EIS experiments.

Adapted from [26].

**Table 2. 2** delivers the results of the fitted  $R_2$  for various structural metals immersed in BOs produced from different biomass sources (pine whitewood and pine residues as low and high ash sources, respectively), as reported by previous studies. Keiser et al. [29] found that SS 430 and SS 430F presented higher corrosion resistance to HAHM BO than 2.25Cr-1Mo, which had lower

$R_2$  [29]. Similarly, Jun et al. [31] also determined, through repeated EIS tests at different times, that SS 430 and SS 430F were more resistant to corrosion than 2.25Cr-1Mo in a HAHM BO environment. They observed that despite SS 430F having a higher density of sulphide inclusions, due to its high sulphur content compared to SS 430, both ferritic SSs showed similar resistance to BO constituents [31].

Furthermore, Jun et al. [32] performed EIS experiments on chromoly steels in HAHM and LALM BOs for up to 19.5 hours. They observed a consistent corrosion reaction of steels over time, and reported similar  $R_2$  values for both HAHM and LALM BOs [32]. The three steels tested with different Cr content: 2.25, 5, and 9 wt.% presented a relatively low  $R_2$ , indicating that they were susceptible to corrosion reaction under both HAHM and LALM BO. Therefore, the authors suggested that steels with higher Cr content, such as SSs, may exhibit higher corrosion resistance against BO constituents [32].

**Table 2. 2.** Previous results of EC tests in a BO environment.

Alloy	Environment	Temperature (°C)	Time (h)	EC type	Fitted $R_2$ (ohm.cm <sup>2</sup> )	Ref (s)
2.25Cr-1Mo	HAHM BO	RT	1	EIS	*6.0×10 <sup>2</sup>	[31]
			18		*1.3×10 <sup>3</sup>	
			118		*3.6×10 <sup>3</sup>	
	LALM BO	RT	1	5.9×10 <sup>2</sup>	[29]	
			2	1.8×10 <sup>3</sup>	[32]	
		19.5	2.2×10 <sup>3</sup>			

5Cr-1Mo	HAHM BO	2	$*7.2 \times 10^2$	
		19.5	$*1.3 \times 10^3$	
	LALM BO	2	$*1.3 \times 10^3$	
		19.5	$*1.7 \times 10^3$	
9Cr-1Mo	HAHM BO	1	$*4.9 \times 10^2$	
		15	$*6.0 \times 10^2$	
	LALM BO	2	$*7.5 \times 10^2$	
		19.5	$*9.0 \times 10^2$	
SS 430	HAHM BO	1	$*2.0 \times 10^5$	[31]
		22	$*1.5 \times 10^6$	
SS 430F	HAHM BO	1	$2.0 \times 10^5$	[29]
		1	$2.6 \times 10^5$	
		1	$*2.8 \times 10^5$	[31]
		20	$*1.7 \times 10^6$	
		170	$*6.0 \times 10^6$	

Note: H, L, A, M stand for high, low, ash, and moisture, respectively. The metal compositions can be found in Appendix A. \* Results are a close approximation from figures.

## 2. 2 CORROSION IN BO AND ITS BLENDS WITH PETROLEUM FRACTIONS

As discussed in **Chapter 1**, upgrading BO can be achieved through co-processing with petroleum intermediates like VGO in FCC units. Several studies have investigated the corrosiveness of BO and petroleum fraction blends by conducting immersion experiments on metals commonly used in refining operations. For example, Keiser et al. [29] conducted immersion experiments for CS, 2.25Cr-1Mo and SSs (201, 304L, 316L, and 409) at 50 °C for 500 hours in different environments to observe the effect of BO on the corrosiveness of fossil intermediates.

The study included a control test using heavy fuel oil (HFO) as a reference and a blend of 50 wt.% HAHM BO/50 wt.% HFO. The authors reported that metals exhibited higher corrosion susceptibility in the blend, indicating the higher corrosivity of BO compared to traditional fossil fuels [29]. The corrosion rate of CS less than 0.01 mm/y in 100 wt.% HFO, but it increased to 0.03 mm/y in the blend. Similarly, the corrosion rate of 2.25Cr-1Mo and SS 409 increased from <0.01 to 0.04 mm/y in HFO and in the blend, respectively. The impact of BO addition on SS 304L and SS 316L could not be determined due to their high resistance at 50 °C, which showed less than 0.01 mm/y in both environments [29].

Brady et al. [33] conducted a study to assess the corrosivity of BO and petroleum blends on various grades of SSs. The authors evaluated corrosion rates of metals by immersion experiments at 525 and 550 °C for 57 and 75 hours in an FCC pilot plant, using 3–10 wt.% HDO BO/90–97 wt.% VGO. Upon analysis of the corrosion products, a multi-layered oxide rich in iron (Fe) was observed in the SSs (201, 304L, 316L, 317L, 409L, and 410) instead of the expected chromia ( $\text{Cr}_2\text{O}_3$ ). The presence of this oxide increased with the Cr content in the metal. Interestingly, the study found that SS 201 exhibited lower corrosion susceptibility than the more expensive SS 300 series. They also observed that the austenitic SS 304L and SS 316L were susceptible to internal attacks through grain boundaries due to the formation of Cr-sulfides caused by the high sulfur content in co-FCC environments. This was attributed to the selective leaching of Cr. In contrast, SS 201, with higher Mn content, did not exhibit intergranular attack as Mn-sulfides formed over Cr-S, leaving more Cr available for passivating the metal. The authors recommended future studies with longer exposure times to better understand the corrosion kinetics in SSs.

**Table 2. 3.** Previous results of immersion test in BO/fossil fuel intermediates blends.

Alloy	Environment	Temperature (°C)	Time (h)	Corrosion rate (mm/y)	Ref (s)
1018 CS	HFO	50	500	<0.01	[29]
	50 wt.% HAHM BO/50 wt.% HFO			0.03	
2.25Cr-1Mo	HFO	50	500	<0.01	[29]
	50 wt.% HAHM BO/50 wt.% HFO			0.04	
SS 201	3–10 wt.% HDO BO/90–97 wt.% VGO	370	70	Corrosion products	[33]
SS 304L	HFO	50	500	<0.01	[29]
	50 wt.% HAHM BO/50 wt.% HFO			<0.01	
SS 316L	3–10 wt.% HDO BO/90–97 wt.% VGO	370	70	Corrosion products	[33]
	HFO			<0.01	
SS 317L	50 wt.% HAHM BO/50 wt.% HFO	50	500	<0.01	[29]
	3–10 wt.% HDO BO/90–97 wt.% VGO			Corrosion products	
SS 409	HFO	50	500	<0.01	[29]
	50 wt.% HAHM BO/50 wt.% HFO			0.04	
SS 410	3–10 wt.% HDO BO/90–97 wt.% VGO	370	70	Corrosion products	[33]

Note: H, L, A, M stand for high, low, ash, and moisture, respectively. The metal compositions can be found in Appendix A. \* Results are a close approximation from figures.

## 2.3 CORROSION IN MODEL BOs

In addition to evaluating the corrosion resistance of structural steels in raw BO and FCC feedstocks (VGO or HFO), it is important to identify the specific BO constituents that contribute to it and to either remove or reduce them prior to upgrading [10]. To this end, Connatser et al. [10] identified the most prevalent BO constituents: acetic acid, formic acid, acetol, levulinic acid, methyl levulinate, ethyl levulinate, glyoxal, methyl glyoxal, guaiacol, glycolic acid, dihydroxyacetone, catechol, 3-methyl-1,2-cyclopentanedione, furfural, cresol, vanillic acid, apocynin, and lactobionic acid [10]. By using the identified BO constituents, researchers can create model BOs with known compositions that can be used for further testing and analysis. This allows for a better understanding of the specific constituents that contribute to corrosion and other undesirable effects and can help in the development of more effective mitigation strategies.

Several authors have evaluated the corrosion resistance of structural steels in model BOs through EIS. Typically, these model BOs consist of 0.1 M of the solute (BO constituent) in a base solution containing 85 wt.% deionized water (DI) and 15 wt.% ethanol [10], [15], [26], [32]. For example, Jun et al. [26] conducted EIS experiments on Cr-Mo steels (2.25Cr-1Mo and 9Cr-1Mo) and ferritic SSs (410 and 430) in solutions of catechol, formic and lactobionic acid for less than 3 hours at RT. They found that 2.25Cr-1Mo had poor corrosion resistance in all organic constituents, which is concluded due to the lower  $R_2$ . It obtained  $1.1 \times 10^3$ ,  $1.2 \times 10^2$ , and  $1.9 \times 10^2$  ohm.cm<sup>2</sup> in 0.1 M catechol, 0.1 M formic and 0.1M lactobionic acid, respectively. Similar behaviour was observed for 9Cr-1Mo presenting corrosion susceptibility in formic and lactobionic acid solutions. However, it was resistant to 0.1 M catechol ( $4.0 \times 10^5$  ohm.cm<sup>2</sup>). Thus, the authors hypothesized that there is

a critical Cr content in steels between 2.25 and 9 wt.% to withstand catechol [26]. On the other hand, the ferritic SSs 410 and 430 exhibited higher corrosion resistance than Cr-Mo steels, based on the  $R_2$ . They showed an  $R_2 > 1 \times 10^5$  ohm.cm<sup>2</sup> for all solutions tested. Based on the results obtained, authors attributed the higher corrosion resistance of ferritic stainless steels to the formation of a Cr-rich passive film, which provides better protection against the corrosive BO constituents such as formic and lactobionic acid. Therefore, it is recommended to use ferritic stainless steels with a Cr content higher than 11 wt.% instead of Cr-Mo steels for storing BOs containing these constituents, even though they are more expensive [26].

Jun et al. [32] also conducted EIS experiments on various grades of Cr-Mo steels in a model BO consisting of 10 wt.% catechol in the previously mentioned base solution. The experiments took place at RT and for different immersion times, up to 19.5 hours. 2.25Cr-1Mo, the steel with the lowest Cr content among the tested metals, one more time behaved poorly showing an  $R_2 < 1 \times 10^3$  ohm.cm<sup>2</sup> at different immersion times [32]. In contrast, 5Cr-1Mo exhibited a higher  $R_2$  value than 2.25Cr-1Mo, it obtained  $7.0 \times 10^3$  ohm.cm<sup>2</sup> for 2 hours, and its corrosion resistance was falling as much as the time increased, ending with an  $R_2$  value of  $1.5 \times 10^3$  ohm.cm<sup>2</sup> for 19.5 hours. Although 5Cr-1Mo showed less corrosion susceptibility in the catechol solution than 2.25Cr-1Mo, it still did not exhibit an acceptable level of resistance [32]. On the contrary, 9Cr-1Mo seemed to have the proper Cr content to withstand the catechol environment. Throughout all immersion times, 9Cr-1Mo displayed an  $R_2 > 1 \times 10^4$  ohm.cm<sup>2</sup>, and this value was decreasing as immersion time increased; proving that the immersion time is detrimental to the steel corrosion resistance. Thus, the authors identified a critical Cr content between 5 and 9 wt.% below which Cr-Mo steels are not suitable for storing BOs with high catechol content [32].

**Table 2. 4.** Previous results of immersion test in model BOs environments.

Alloy	Environment	Temperature (°C)	Time (h)	EC type	Fitted R <sub>2</sub> (ohm.cm <sup>2</sup> )	Ref (s)	
2.25Cr- 1Mo	0.1 M catechol **	RT	<3	EIS	*1.1×10 <sup>3</sup>	[26]	
	0.1 M formic acid **				*1.2×10 <sup>2</sup>		
	0.1 M lactobionic acid **				*1.9×10 <sup>2</sup>		
	0.1 M catechol+0.05 M formic acid **				*2.7×10 <sup>2</sup>		
	0.1 M catechol+0.1 M formic acid **				*2.1×10 <sup>2</sup>		
5Cr- 1Mo	0.05 M catechol+0.1 formic acid **	RT	2	EIS	*2.0×10 <sup>2</sup>	[32]	
	10 wt.% catechol **				*7.0×10 <sup>3</sup>		
					5.5		*3.0×10 <sup>3</sup>
					11		*4.0×10 <sup>3</sup>
					19.5		*1.5×10 <sup>3</sup>
					2		*2.8×10 <sup>4</sup>
					5.5		*1.4×10 <sup>4</sup>
					11		*1.4×10 <sup>4</sup>
19.5	*1.7×10 <sup>4</sup>						
9Cr- 1Mo	0.1 M catechol **	RT	<3	EIS	*4.0×10 <sup>5</sup>	[26]	
	0.1 M formic acid **				*4.5×10 <sup>2</sup>		
	0.1 M lactobionic acid **				*7.0×10 <sup>2</sup>		
	0.1 M catechol+0.05 M formic acid **				*6.5×10 <sup>2</sup>		
	0.1 M catechol+0.1 M formic acid **				*4.5×10 <sup>2</sup>		

	0.05 M catechol+0.1 M formic acid **		$*5.0 \times 10^2$	
SS 201	0.1 M catechol **		$1.1 \times 10^6$	
	0.1 M formic acid **		$4.3 \times 10^6$	
	0.1 M lactobionic acid **		$5.5 \times 10^5$	
	0.1 M catechol+0.1 M formic acid **	2-15	$2.7 \times 10^6$	[15]
	0.1 M catechol **		$5.5 \times 10^5$	
SS 316L	0.1 M formic acid **		$9.9 \times 10^5$	
SS 410	0.1 M catechol **		$*1.0 \times 10^6$	
	0.1 M formic acid **		$*3.0 \times 10^5$	
	0.1 M lactobionic acid **		$*3.5 \times 10^5$	
	0.1 M catechol+0.05 M formic acid **	<3	$*1.5 \times 10^5$	[26]
	0.1 M catechol+0.1 M formic acid **		$*2.3 \times 10^5$	
	0.05 M catechol+0.1 M formic acid **		$*1.1 \times 10^5$	
	0.1 M catechol **		$1.6 \times 10^6$	
	0.1 M formic acid **		$4.4 \times 10^5$	
	0.1 M lactobionic acid **	2-15	$7.6 \times 10^4$	[15]
	0.1 M catechol+0.1 M formic acid **		$2.6 \times 10^5$	
SS 410	0.1 M lactobionic acid **		$*8.0 \times 10^4$	
	0.1 M catechol **	21	$*1.5 \times 10^6$	[10]
	0.1 M formic acid **		$*1.8 \times 10^6$	

	0.1 M glycolic acid **		$*1.8 \times 10^6$	
	0.1 M acetic acid **		$*2.0 \times 10^6$	
	0.1 M 3-methyl-1, 2-cyclopentanedione **		$*2.0 \times 10^6$	
	0.1 M levulinic acid **		$*2.5 \times 10^6$	
	0.1 M dihydroxy acetone **		$*3.0 \times 10^6$	
	0.1 M acetol **		$*3.0 \times 10^6$	
	0.1 M guaiacol **		$*4.0 \times 10^6$	
	0.1 M methyl levulinate **		$*6.5 \times 10^6$	
	0.1 M cresol **		$*6.5 \times 10^6$	
	0.1 M glyoxal **		$*9.5 \times 10^6$	
	0.1 M furfural **		$*1.0 \times 10^7$	
	0.1 M ethyl levulinate **		$*1.0 \times 10^7$	
	0.1 M methyl glyoxal **		$*1.1 \times 10^7$	
	0.1 M catechol **		$*4.0 \times 10^5$	
	0.1 M formic acid **		$*3.6 \times 10^5$	
	0.1 M lactobionic acid **		$*4.1 \times 10^5$	
SS 430	0.1 M catechol+0.05 M formic acid **	<3	$*2.2 \times 10^5$	[26]
	0.1 M catechol+0.1 M formic acid **		$*2.9 \times 10^5$	
	0.05 M catechol+0.1 M formic acid **		$*2.0 \times 10^5$	

Note: The metal compositions can be found in Appendix A. \* Results are a close approximation from figures. \*\* Base solution: 85 wt.% deionized water (DI) and 15 wt.% ethanol.

Acknowledging that SSs are more resistant to BO degradation than Cr-Mo steels, Connatser et al. [10] carried out EIS measurements on SS 410 disks in the different types of BO constituents they had identified earlier. They observed that some constituents such as, furfural, ethyl levulinate and methyl glyoxal were not aggressive to the SS 410 coupons since the global resistance of the passive film ( $R_2$ ) was several orders of magnitude higher than those reported for SSs in passive state ( $8 \times 10^5 \text{ ohm.cm}^2$ ), as indicated in **Table 2. 4**. Other constituents, except for the sugar acid, lactobionic, were slightly aggressive to the passive film, as lower  $R_2$  were reported [10]. The resistance against charge transfer under lactobionic acid was the lowest among the BO constituents studied. Implying that the passive film is not stable at room temperature under this large sugar acid [10]. The authors attribute the loss of the passivating state to lactobionic acid acting as a chelating agent, leaching iron from the alloy. Therefore, they proposed conducting further EIS assessment with different alloys to identify a better candidate for storing BO constituents. The results of such experiments could provide valuable information for the development/identifying of new materials with improved resistance to BO degradation.

## **2. 4 CORROSION IN BO AND ITS BLENDS WITH ADDITIVES**

**Chapter 1** looked into co-processing in FCC units as an upgrading path for BO. The developed direct upgrading techniques reviewed include both physical methods (emulsification and solvent addition) and chemical methods (hydrotreatment, steam reforming, catalytic cracking, and supercritical fluid) [34]. Each method has its obvious advantage and drawbacks. For instance, BO can be deoxygenated in the presence of hydrogen, commonly known as hydrotreating to produce hydrodeoxygenated BO (HDO-BO), but this process is expensive and energy-intensive

[12], [21]. In addition to chemical methods such as FCC co-processing or HDO-BO, several studies have investigated the influence of the addition of solvents as corrosion inhibitors for BO and other biofuels [3], [35], [36]. These solvents can either be added directly to the biofuel or used as a blending agent. The solvents may act as corrosion inhibitors by forming a protective film on the metal surface or by changing the physicochemical properties of the biofuel to reduce its corrosivity. For example, one study investigated the use of alcohols and glycols as corrosion inhibitors for biofuels [37]. The results showed that the addition of these solvents to the biofuels significantly reduced their corrosivity towards steel and other metals. Another study investigated the use of 2-ethylhexanol as a blending agent for diesel and biodiesel fuels. The results showed that the addition of 2-ethylhexanol improved the lubricity and reduced the corrosivity of the blended fuels [38].

In addition to inhibiting corrosivity, researchers also found that adding alcohols to BO can enhance its thermal instability by forming lighter-molecular-weight compounds. Shawal et al. [36] investigated the influence of alumina ( $\text{Al}_2\text{O}_3$ ) on corrosivity when added to palm-derived BO. Immersion experiments were performed at 50 °C for 3, 6 and 12 hours. Corrosion rates of 3.55, 9.03, and 23.98  $\text{g}/\text{cm}^2\text{y}$  for 3, 6, and 12 hours were reported, respectively, when alumina was added to BO. Instead, higher corrosion rates were observed in raw BO: 4.15  $\text{g}/\text{cm}^2\text{y}$  for 3 hours, 13.67 for 6 hours, and 25.54 for 12 hours. The authors explained that the corrosivity of BO is reduced due to alumina lowers BO acidity [36].

A similar study was conducted by Wang et al. [3], they investigated the influence of adding methanol not just for the BO thermal stability but also on its corrosivity. They added up to 20 wt.% of methanol to BO and performed immersion experiments at 50 and 80 °C for 168 hours [3]. Post-immersion, they observed that as much as methanol is added to the mixture at 80 °C, the corrosion rate in SS 304L lowered compared to blank tests without methanol (**Table 2. 1**), as indicated in **Table 2. 5**. The corrosion rate dropped to less than 0.1 mm/y when adding 20 wt.% of methanol, which is a significant corrosion resistance increase, considering than this SS exhibited 0.8 mm/y in raw BO at the same immersion temperature and time [3]. SS 316L performed very well under raw BO at 50 and 80 °C. Hence, the addition of methanol to BO was found to be irrelevant in this case. In Wang et al. [3]' work, an unexpected finding was observed in the immersion experiments of CS. The addition of methanol to BO was anticipated to lower the BO corrosivity in CS, since the authors performed a benchmark immersion experiment in a mixture of water and methanol. As much as methanol was added to water, the corrosion rate of CS lowered. However, this behaviour was not exhibited in mixtures of BO and methanol neither at 50 °C nor at 80 °C. Instead, the corrosion susceptibility of CS increased when adding methanol BO at 50 °C, and it showed a parabolic behaviour at 80 °C. Reaching a maximum when adding 10 wt.% of methanol. The authors explained that this behaviour could be attributed to the chelation effect of some of the oxygenated compounds within BO, mentioned above. Hence, the addition of methanol decreases the BO viscosity allowing higher diffusivity of oxidants and chelate complexes, increasing the corrosion rate in CS. However, as methanol concentration increases some of the chelate complexes could be deposited on the CS surface, which apparently lowers the corrosion rate [3].

Biomass-derived BO is not the only biofuel that needs upgrading, used cooking oil or UCO, is a valuable biofuel that can be recycled and converted into useful products. When UCO is collected and processed, it can be converted into biodiesel. Normally, the predecessor of UCOs are vegetable-based oils [36]. Bruun et al. [35] studied the inhibition mechanism of different amino acids added to UCO. After performing immersion experiments at room temperature in a CS, they observed that low concentration (as low as 160 ppm) of L-Lycine or L-Arginine can drastically drop the amount of Fe concentration dissolved in the UCO. Post-immersion, they found a concentration of Fe dissolved to be higher than 390 ppm, however, when adding the amino acids, the Fe dissolved was approximately less than 20 ppm. They explained that the inhibition mechanism was owe to both amino acids prevent the corrosion by blocking the cathodic reaction [35].

**Table 2. 5.** Previous results of immersion test in a BO with corrosion inhibitors environment.

<b>Alloy</b>	<b>Environment</b>	<b>Temperature (°C)</b>	<b>Time (h)</b>	<b>Corrosion rate (mm/y)</b>	<b>Ref (s)</b>
A36 CS	Pine BO/5 wt.% methanol	50	168	*1.65	[3]
	Pine BO/10 wt.% methanol			*1.85	
	Pine BO/15 wt.% methanol			*1.92	
	Pine BO/20 wt.% methanol			2.0	
	Pine BO/5 wt.% methanol			80	

	Pine BO/10 wt.% methanol			8.1	
	Pine BO/15 wt.% methanol			*7.8	
	Pine BO/20 wt.% methanol			6.8	
CS	10g Palm BO/1.5g AL2O3	50	3	3.55 g/cm <sup>2</sup> y	[36]
			6	9.03 g/cm <sup>2</sup> y	
			12	23.98 g/cm <sup>2</sup> y	
H44 CS	UCO/160 ppm L- Lycine	RT	72	*<20 ppm of Fe	[35]
	UCO/160 ppm L- Arginine			*<20 ppm of Fe	
SS 304L	Pine BO/5 wt.% methanol			*0.6	
	Pine BO/10 wt.% methanol			*0.5	
	Pine BO/15 wt.% methanol	80	168	*0.3	[3]
	Pine BO/20 wt.% methanol			*<0.1	
SS 316L	Pine BO/5, 10, 15, and 20 wt.% methanol			<0.1	

*Note: The metal compositions can be found in Appendix A. \* Results are a close approximation from figures.*

## 2. 5 SUMMARY OF CORROSION CHALLENGES

When using structural steels in a co-FCC environment, it is crucial to consider factors such as the composition of the steel and the conditions under which it will be exposed to the BO blends. One important factor to consider is the Cr content of the steel. Studies have shown that steels with a Cr content greater than 9 wt.% are able to withstand exposure to BO under storage conditions. Some authors have even suggested that a minimum Cr content of 11wt.% is necessary to ensure durability, under those conditions. However, the Cr content is not the only alloying element to consider, studies have reported that Ni, Mo, and Mn content also improve the corrosion resistance of the steels. Another important factor is the duration of the exposure of steel to the BO or BO/fossil intermediates blends, as immersion time has been shown to increase the rate of corrosion.

Despite the importance of these factors, it is worth noting that testing the effects of BO on steels can be challenging, especially at higher temperatures. EC tests, for example, are not the easiest way to carry out experiments at high temperatures, such as the ones in the FCC feeding system. Most of the corrosion results obtained by previous authors using EC tests are limited to RTs. In contrast, some authors have carried out immersion experiments in CSs, Chromoly Steels, and SSs up to just 80 °C in BO and BO/fossil intermediates blends. To accurately test the effects of BO on steel, immersion experiments are preferred over EIS for high temperature conditions. In conclusion, when choosing a steel for use in co-processing environments, it is important to consider factors such as the Cr, Ni, Mo, and Mn content, and immersion time. Furthermore, it is crucial to choose the right method of testing to accurately assess the effects of BO on the steel.

While EC tests have limitations, immersion experiments are preferred for high temperature conditions.

# CHAPTER 3 EXPERIMENTAL PROCEDURES

This section describes the experimental procedure used in this study. The study design, materials, and methods used in the experiment are outlined in detail. The procedure includes steps for preparing the metal coupons, conducting the experiments, and characterizing post-experiment samples. The specific techniques and equipment used in the study are also discussed.

## 3.1 PREPARATION OF METAL COUPONS

The preparation of metal coupons for corrosion immersion experiments is a crucial step in ensuring the validity of the results. In this study, corrosion samples with dimensions of 1 x 1/4 x 1/16 in<sup>3</sup> were machined from several commonly used structural metals in the oil and gas industry. These metals include commercial grade CS (A36), chromoly steel (P91), SS 304L, SS 316L and a nickel-based superalloy (HX), their corresponding compositions are listed in **Table 3.1**. The selection of these metals was based on their widespread use in various oil and gas processes, such as co-processing in FCC units, which are known to be highly corrosive environments [5], [25]. After obtaining coupons with the desired dimensions, the surfaces and edges were polished to a 600-grit finish using SiC paper. This is helpful to remove any surface contaminants and imperfections that may affect the corrosion rate. The polishing process was done with great care to ensure that the surface of the coupons was smooth and uniform.

**Table 3. 1.** Chemical compositions (wt.%) of selected structural metals.

<b>Alloy</b>	<b>Fe</b>	<b>C</b>	<b>Cr</b>	<b>Cu</b>	<b>Mn</b>	<b>Mo</b>	<b>Ni</b>	<b>P</b>	<b>Si</b>	<b>S</b>	<b>Other</b>
<b>CS</b>	Bal.	0.2	0.05	0.04	0.74	0.01	0.01	0.01	0.01	0.01	V,0.002
<b>P91</b>	Bal.	0.1	8.94	0.06	0.37	0.91	0.11	0.02	0.3	0.01	V,0.18; Nb, 0.06
<b>SS 304L</b>	Bal.	0.03	18.3	0.5	1.61	0.34	8.06	0.03	0.34	0.01	N, 0.06
<b>SS 316L</b>	Bal.	0.02	16.6	0.55	1.45	2.03	10.1	0.03	0.37	0.01	N, 0.04; Co, 0.41
<b>HX</b>	19.7	0.06	21.5	0.08	0.66	8.38	Bal.	0.01	0.25	0.01	Ti, 0.1; Co, 1.20

After polishing, the coupons were rinsed with deionized (DI) water to remove any remaining particles or debris. The coupons were dried using compressed air to ensure that they were completely dry before being weighed. Drying the coupons is important as any trapped DI water can lead to inaccurate weight measurements during the immersion experiments. Once the coupons were prepared, their weight was recorded using a microbalance.

### 3. 2 IMMERSION EXPERIMENTS SET-UP

The immersion experiments were designed to investigate the corrosion behavior of various metals in a pinewood-derived BO environment. The experiments were performed in accordance with the ASTM G31 standard, which is a widely accepted method for evaluating the resistance of metals to corrosion in aqueous environments [39]. The experiments were conducted at temperatures of 80, 150, and 220 °C for a duration of 24 hours, with an additional immersion experiment for two specific metals, CS and P91, for a shorter duration of 10 hours. To ensure the validity of the results, two coupons of each metal were used at each temperature. Due to limitations

in the amount of BO available, the immersion experiments were set up in pairs. SS samples were immersed together, P91 and HX were immersed together, and CS samples were immersed individually. This configuration was selected to ensure that the metals with high susceptibility to BO corrosivity were immersed with high corrosion resistance metals (e.g., P91 and HX).

The metal strip coupons were affixed to a PTFE holder and placed inside a cylindrical PTFE container with a capacity of 490 mL. The samples were immersed in 200 mL of BO for the duration of the experiment. The whole setup was placed inside an autoclave, specifically an Intelligent Magnetic Heating Stirrer, which provided precise control over the temperature and duration of the experiments. The autoclave was sealed by securely fastening the security bolts and closing the valves, as illustrated in **Figure 3. 1**. The immersion time was calculated from the moment the desired temperature conditions were reached. The system typically took approximately 25, 35, and 50 minutes to reach temperatures of 80, 150, and 220 °C, respectively. A thermocouple was inserted through the top of the autoclave to monitor the temperature throughout the entire experiment, as depicted by the white cord in **Figure 3. 1-a and b**. Additionally, pressure gauges were used to monitor changes in pressure. The autoclave was heated uniformly through an outer coil jacket. Upon completion of the experiments, each sample was gently cleaned with ethanol using Q-tips to remove surface corrosion products. The metal strip coupons were also cleaned in an ultrasonic bath with ethanol and DI water, for a duration of 10 minutes each. The metal coupons were dried, and their final weight was recorded. The corrosion rates (CR) were calculated using **Equation 3. 1**, which considers the density of the metal ( $D$ -g/cm<sup>3</sup>), the surface area of the coupon ( $A_r$ -cm<sup>2</sup>), the weight loss ( $W$ -g), the time of exposure ( $t$ -h), and a constant ( $K$ ) of 87600 mm y<sup>-1</sup> cm<sup>-1</sup> [40].

$$CR \left( \frac{mm}{y} \right) = \frac{K \times W}{Ar \times t \times D} \quad (3.1)$$

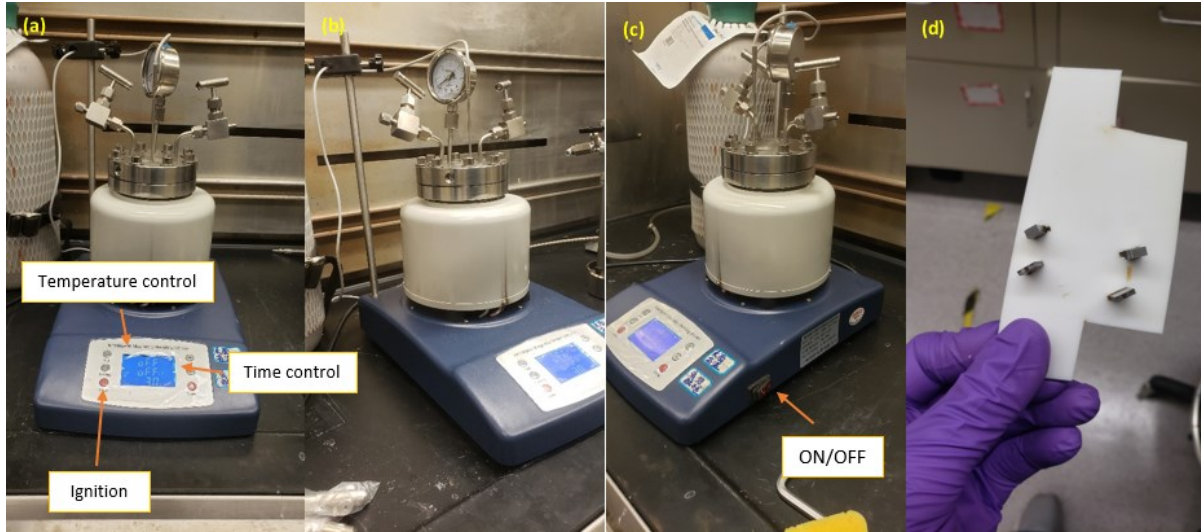


**Figure 3. 1.** The apparatus used for immersion and aging experiments. (a) front view; (b) left view; (c) right view; and (d) metal coupons anchored to PTFE holder before immersion.

The properties of the BO used in the experiments are outlined in **Table 3. 2**. A rotational rheometer or viscometer (Brookfield DV-IIIITM Ultra Rheometer) was used to measure its viscosity, which is the resistance of the liquid (BO) to flow. The rheometer works by rotating a spindle, or rotor, in the BO at a fixed temperature. In this study, all the viscosities were measured at RT. The torque required to rotate the spindle is measured and used to calculate the viscosity of the BO [34], [41]. The resulting viscosity value obtained for BO stock was 189.3 cP. Furthermore, The Anton Paar DMA 35 Density Meter was utilized to determine the density of BO. The instrument employs a precise oscillating piston immersed in the BO sample. The piston oscillates at a constant frequency, and the density of the liquid is calculated based on the oscillation frequency. The oscillation frequency is measured using a piezoelectric sensor, which converts the mechanical oscillations of the piston into an electrical signal. The electrical signal is subsequently

processed by the microcontroller of the device to calculate the density of the BO (1.21 g/mL) [42]. Three measurements were taken, and the final value was determined through averaging.

The Mettler Toledo C10SC Coulometric KF Titrator was employed to determine the water content in BO. The method of analysis is based on the Karl Fischer titration, a volumetric method that utilizes a reagent to react with water present in the sample. The BO sample was diluted 100 times with methanol, and then placed in the titration cell. An electric current was passed through the cell, and the reagent was added incrementally until all water in the sample was consumed, as indicated by a change in the electrical current. The amount of reagent consumed was found to be directly proportional to the amount of water in the sample [34], [43]. Thus, the water content of the BO sample, measured as 23.6 wt.%, was determined after deducting the water content found in the methanol solvent [3]. In addition, the pH meter Thermo Scientific™ Orion Star A211 was used to measure the acidity of BO. The apparatus makes it possible by measuring the electrical potential difference between a pH electrode and a reference electrode. The pH electrode is a glass electrode that is sensitive to hydrogen ions ( $H^+$ ) in the solution, while the reference electrode is a stable electrode that maintains a constant potential [34], [44]. Similar to the viscosity and density measurements, the acidity of the BO was determined by averaging the results of three consecutive measurements, yielding a final value of 2.39.

The procedure for measuring ash content in BO began by weighing a 15 mg sample, which was then placed in a crucible. The crucible was inserted in a muffle furnace, which was preheated to 775 °C and held at that temperature for 20 minutes. The furnace was set to have flowing air to

maintain a controlled environment and to avoid oxidation or other reactions in the sample. After this time and temperature, the crucible was removed from the furnace and allowed to cool to RT. The sample was then weighed again to determine the weight of the remaining ash. The ash content was calculated as the weight of the ash divided by the initial weight of the sample, multiplied by 100 to express the result as a percentage (0.05 wt.%) [3], [34]. Finally, an elemental analysis was performed using the Thermo Scientific™ FLASH 2000 CHNS/O Analyzer. The BO sample was introduced into the instrument and combusted in a controlled oxygen environment in the combustion chamber. The weight percentage of carbon (C), hydrogen (H), sulfur (S), and nitrogen (N) were determined, and the oxygen (O) content (43.89 wt.%) was calculated by difference as the remainder of the weight percentages of the other elements [3], [5], [34]. Once the properties of BO are obtained, the low heating value (LHV) can be calculated through the Dulong's formula, that considers the C, H, S, O, N, and water content [3], [34], [45].

**Table 3. 2.** Properties of BO used in immersion and aging experiments.

<b>Property</b>	<b>Value</b>	<b>Equipment</b>
Viscosity	189.3 cP	Brookfield DV-III™ Ultra Rheometer
Density	1.21 g/mL	Anton Paar DMA 35 Density Meter
Water content	23.6 wt.%	Mettler Toledo C10SCoulometric KF Titrator
pH value	2.39	Thermo Scientific™ Orion Star A211
Ash content	0.05 wt.%	Muffle Furnace
Heating Value	18.9 MJ/Kg	Dulong's formula
Elemental analysis (wt.%): C (48.37), H (7.50), N (0.23), S (0), O (43.89)		Thermo Scientific™ FLASH 2000 CHNS/O Analyzers

### 3. 3 IMMERSED SAMPLES POST-CHARACTERIZATION

The process of analyzing the microstructures of the metals began by preparing the samples. Coupons were cut from the five metals studied. These coupons were then cold mounted in epoxy and polished using SiC paper until they reached a grit of 1220. The samples were then polished further using a diamond suspension solution until reaching a final polishing solution of 1 micron. Once polished, the samples were cleaned and dried for further analysis. To determine the initial microstructures of the metals, the samples were etched using a specific etchant for each metal. The CS was etched with Nital, the SS 304L and SS 316L were etched with Adler's etchant. After that, the microstructures were analyzed using optical micrography (OM), as illustrated in **Figure 3. 2**. OM is a technique that uses visible light to capture an image of the microstructure of a material [46]. The images captured by OM allowed for a detailed analysis of the microstructure, including the size, shape, and distribution of the various phases present in the material. The microstructures of the different metals were analyzed in order to understand their properties and behavior in a specific condition.

The CS microstructure is composed of a combination of ferrite and pearlite. Ferrite is a body-centered cubic crystal structure, which is a solid solution of iron and carbon. Pearlite, on the other hand, is composed of alternating layers of ferrite and cementite ( $\text{Fe}_3\text{C}$ ), which is a hard and brittle intermetallic compound [47]. The presence of pearlite in the microstructure of CS provides the material with a unique combination of strength and ductility. The P91 microstructure is composed primarily of tempered martensite, which is a hard and brittle phase of iron [48]–[51]. The tempered martensite is formed by quenching the steel from high temperatures and then reheating it to a lower temperature, a process known as tempering. The quenching process causes the steel to transform

from austenite to martensite, which is a very hard and brittle phase. Tempering the martensite causes it to become less brittle and more ductile [47]. Additionally, small amounts of carbides are present in the P91 microstructure, which improve the high-temperature strength and creep resistance of the alloy. The SS 304 and SS 316 microstructures are composed of ferrite clusters within an austenite matrix. Austenite is a face-centered cubic crystal structure, which is a solid solution of iron, nickel and chromium. The ferrite clusters, which are dispersed within the austenite matrix, provide additional strength and improved corrosion resistance [47]. The HX microstructure is characterized by the presence of metal pools contours generated by a laser beam during its production. These contours are the result of the laser beam melting and solidifying certain regions of the material, creating unique microstructural features that contribute to the high-temperature strength and corrosion resistance of the alloy [52]. After the immersion experiments were completed, a thorough characterization of the metal coupons was conducted to analyze the changes in the surface caused by the immersion in the BO environment. The first step in this characterization process was to take photographic images of the metal coupons to visually compare the surface changes with the initial surface of the coupons. These images were also used to identify specific areas of the coupons where corrosion was more severe, which allowed for further analysis using more advanced techniques.

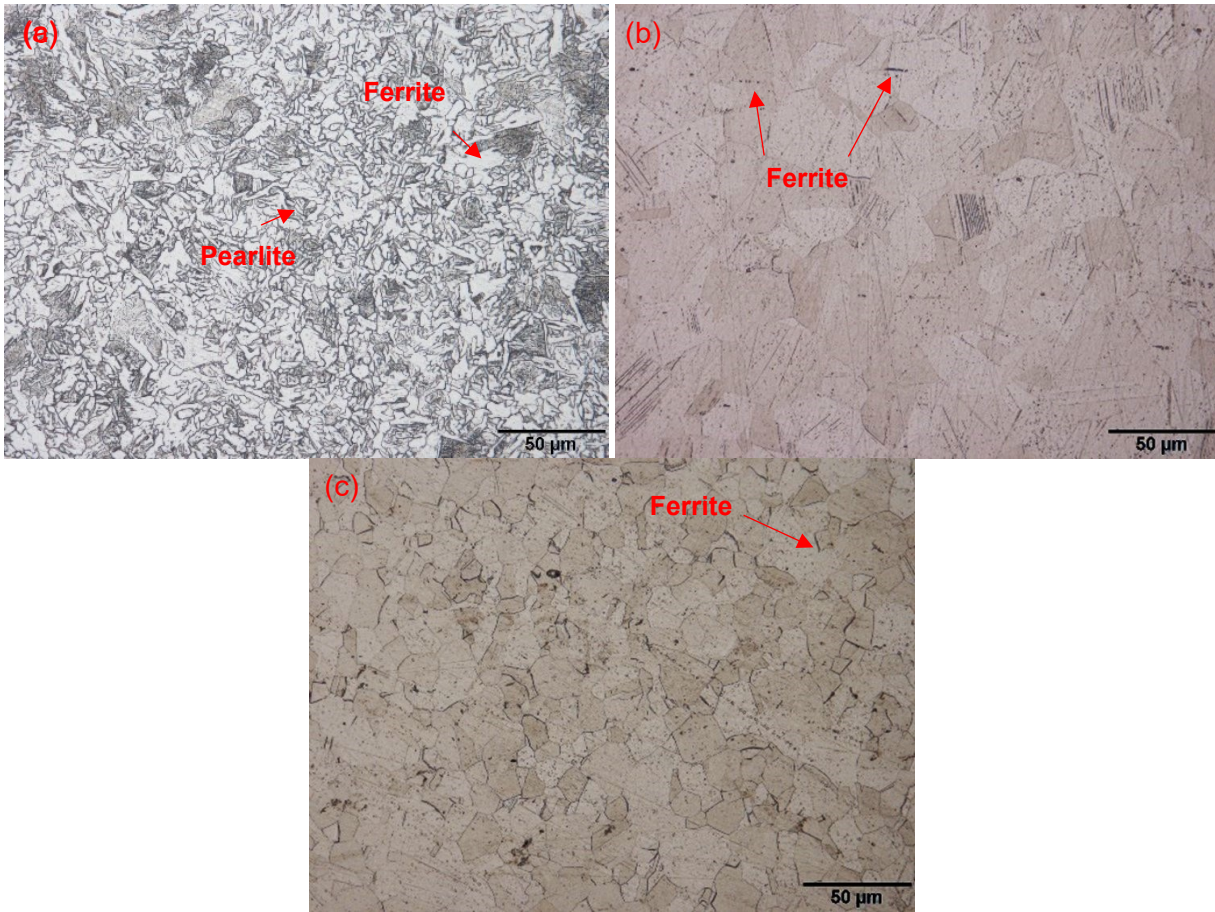


**Figure 3. 2.** Optical micrographs of etched metals used in immersion experiments. (a) CS; (b) SS 304L; and (c) SS 316L. Microstructures of commonly used P91 [48] and HX [52] can be found in the reference.

Scanning Electron Microscopy (SEM) and X-ray diffraction (XRD) were used to gain a deeper understanding of the corrosion process. SEM is a powerful imaging technique that allows for the analysis of the surface structure and composition of a wide range of materials. It works by scanning a focused beam of electrons over the surface of the sample, which causes the electrons in the sample to emit secondary electrons (SE). These SE are detected and used to create an image of the

sample surface [53]. The corroded morphology of the immersed samples was analyzed utilizing the SE imaging mode of SEM due to its ability to provide high-resolution images of the surface structure, allowing for a detailed examination of the corrosion process and identification of any specific corrosion mechanisms that may have occurred. XRD, on the other hand, is a technique that allows for the identification of the specific chemical compounds present in the sample by analyzing the patterns of the X-rays that are diffracted back from the sample. This technique is particularly useful for identifying the phases present in a material and can be used to determine the relative amounts of each phase present. Additionally, XRD can also be used to determine the crystal structure, crystal size, and preferred orientation of the crystals in the sample [54]. In this work, XRD was used to identify the deposited corrosion products after immersion in BO.

Furthermore, the immersed samples were cut in half with a precision saw, followed by cold mounting and mirror polishing to analyze the cross-section through SEM and Energy Dispersive Spectroscopy (EDS). The EDS is a detector that is integrated into the SEM, which can be used to analyze the elemental composition of the sample by measuring the energy of X-rays that are emitted by the sample as a result of the electron beam interacting with it [53]. This allowed for a detailed analysis of the corrosion products formed on the surface of the metals as well as the distribution of the corrosion products within the metal. The results of these analyses were critical in understanding the corrosion behavior of the metals in BO environments. The microstructures of the metals, the corroded morphology, and the chemistry of the corrosion products were important factors in determining the corrosion rate and the durability of the metals in BO environments.

### 3. 4 AGING EXPERIMENTS SET-UP

The aging experiments were meticulously carried out in the same apparatus as the immersion testing, at a temperature of 80, 150, and 220 °C for a duration of 24, 96, and 168 hours to thoroughly investigate the influence of time and temperature on the co-FCC feeding conditions due to BO thermal instability. Furthermore, additional aging experiments were performed at shorter time intervals to determine the critical point at which solid content begins to increase. Specifically, 100 mL samples of BO were carefully placed in PTFE cylindrical container, which were then introduced into the autoclave and sealed to maintain optimal conditions. Following the completion of the experiments, the pressure within the autoclave was recorded and the apparatus was left to cool down for a period of 24 hours. Once cooled, the pressure was again monitored. In addition, two aged samples of 10 mL each were taken from the top and bottom layers to evaluate any changes in physical properties.

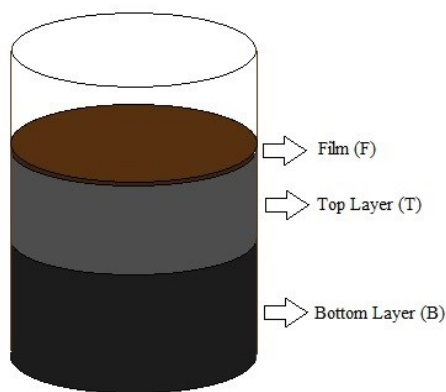


**Figure 3. 3.** Schematic of phase separation in BO aging experiments at 150 °C.

It was observed that during the aging process, two distinct phases were clearly visible, as depicted in **Figure 3. 3**. Any extra film formed over the top layer was collected with the utmost precision using fine tweezers. The weight fraction of the phases formed after the aging experiments were determined by weighing them. The viscosity and density of the samples were measured at 25 °C utilizing the same equipment used to determine the properties of BO in **Table 3. 2**. Finally, thermogravimetric analysis (TGA) was performed on the samples in a flowing argon atmosphere (50 mL/min) using the advanced Thermo Cahn TherMax 300. The BO samples were heated from 30 to 750 °C at a constant rate of 10 °C /min, and the mass losses were tracked to provide a comprehensive analysis of the samples.

# CHAPTER 4 CORROSION OF STEELS IN PYROLYSIS OIL UP TO 220 °C

This section presents the results of comprehensive immersion experiments, which were conducted on five structural metals commonly used in FCC units during co-processing. As co-processing of BO and VGO in FCC units becomes increasingly prevalent, the potential corrosion of FCC hot-end components must be thoroughly investigated due to the high acidity of BO. Despite extensive research on the corrosion of CSs, low-alloy steels and SSs in BO environments at temperatures below 80 °C, the corrosion of these metals at FCC feeding temperatures of 100–300 °C has yet to be fully explored. The results presented in this section aim to evaluate the corrosion resistance of the structural metals in the presence of BO at feeding temperatures up to 220 °C. The results of these experiments provide valuable insights into the potential use and risk assessment of these metals in co-processing applications, and their suitability for use in FCC units. Part of this Chapter has been published and presented as *H. Pedraza, H. Wang, X. Han, Y. Zeng and J. Liu, “Investigating the thermal stability and corrosivity of biocrude oil at FCC feeding temperatures for co-processing applications” AMPP 2023* and *H. Pedraza, H. Wang, X. Han, Y. Zeng and J. Liu, “Corrosion and Aging Risk Assessment of the co-FCC Feed Injection System” Biomass and Bioenergy 2023*.

## 4. 1 CARBON STEEL (CS) A36 IN BO

The first metal chosen for the corrosion studies was CS. Despite its known susceptibility to corrosion, CS is a commonly used structural metal in refining operations, particularly in pipelines, as aforementioned in previous chapters. Before the beginning of the experiments, there was a preconceived notion that at temperatures between 80 and 220 °C under BO, the CS would exhibit poor corrosion resistance. This was assumed due to its lack of alloying elements that can improve its corrosion resistance, as shown in **Table 3. 1** [55]. However, including this metal in the study was necessary to provide a thorough risk assessment when considering the use of CS in co-processing applications. As a result of immersion experiments for 24 hours, it was observed that the corroded coupons underwent a change in colour to a dark-brown hue, as shown in **Figure 4. 1**. Upon comparison to the coupon prior to immersion, it was evident that the surface of the corroded coupons became increasingly rough and dark as the temperature was raised. This suggests that active corrosion occurred at 80 °C under BO conditions. Additionally, as the temperature increased, it was observed that the middle section of the coupons appeared to be thicker than the end sections. This is likely due to the fact that the middle section was attached to the PTFE holder, while the end sections were fully immersed in BO, resulting in a greater degree of weight loss.

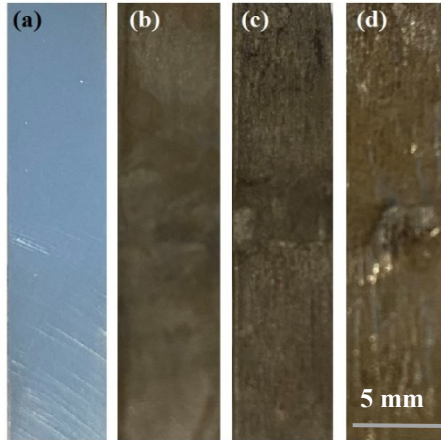


**Figure 4. 1.** Photographic images of CS: (a) before immersion; after immersion for 24 hours in BO (b) at 80 °C, (c) 150 °C, (d) and 220 °C.

CS exhibited high CRs at high temperatures under BO, which was not surprising. At 80 °C for 24 hours, a CR of 11.97 mm/y was observed. This rate increased to 26.15 mm/y at 150 °C and reached a high of 51.96 mm/y at 220 °C. The categorization of CRs in oil production systems can come from various sources, some being more conservative than others, as illustrated in **Table 4. 1**. The excessive corrosion of CS has been previously reported by Wang et al. [3], who also found that when exposed to 80 °C, the CR was 7.20 mm/y. Despite the similar corrosion rates, the use of different equipment in the immersion experiments results in differences between them. They also observed that the samples that were fully immersed in BO exhibited uniform corrosion [3].

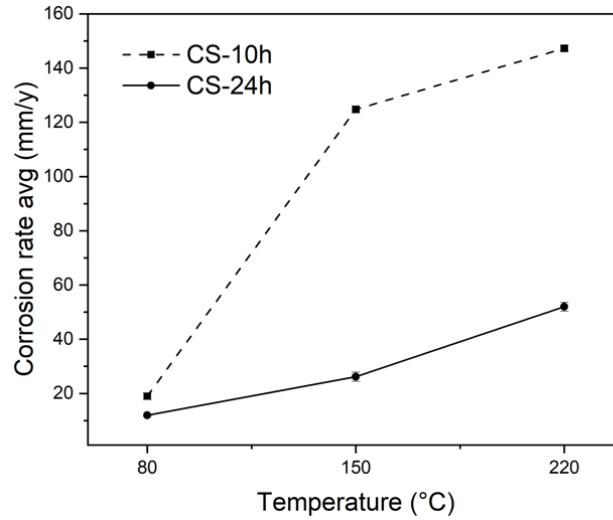


**Figure 4. 2.** The averaged corrosion rates of CS after 10 and 24 hours of immersion in BO at 80 to 220 °C.

**Table 4. 1.** Categorization of corrosion rates in oil production systems, NACE—SP0775-2018 and Bradford et al. (2001) [56], [57].

Corrosion rate average (mm/y)			
NACE—SP0775-2018		Bradford (2001)	
<b>Low</b>	< 0.025	Good	< 0.1 mm/y
<b>Moderate</b>	0.025–0.12	Acceptable	0.1–1
<b>High</b>	0.13–0.25	Excessive	> 1
<b>Severe</b>	> 0.25		

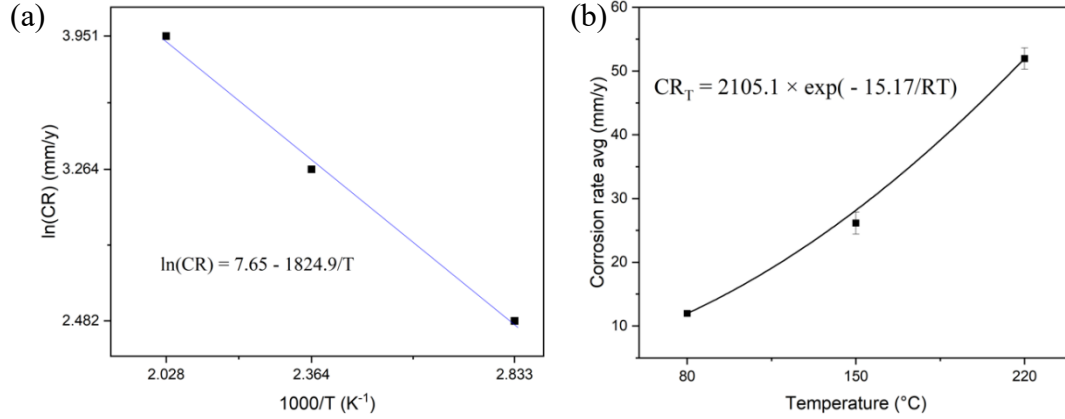


**Figure 4. 3.** Dependence of the corrosion rate of CS on the temperature (80–220 °C) according to the Arrhenius plot for BO, (a) logarithm of the Arrhenius equation, and (b) the Arrhenius equation.

The relationship between CR and temperature is described by the Arrhenius law, as expressed in **Equation 4. 1**. This equation states that the CR is related to temperature through the Arrhenius constant ( $A$ ), the molar activation energy ( $\Delta E$ ) in KJ/mol, the universal gas constant ( $R$ ) with a value of 8.314 J/mol K, and the temperature in K ( $T$ ) [58].

$$\text{CR} = A \times e^{\frac{-\Delta E}{RT}} \quad (4. 1)$$

The molar activation energy of a corrosion process can be determined by applying the natural logarithm to both sides of **Equation 4. 1** and plotting the  $\ln(\text{CR})$  vs  $1/T$  [59]. The molar activation energy can then be calculated from the slope of this plot, as shown in **Figure 4. 3(a)**. The molar activation energy of the corrosion of CS in BO between 80 and 220 °C has been determined to be 15.98 KJ/mol. According to previous research, the molar activation energy of diffusion in water is typically in the range of 10–45 KJ/mol [60]. This implies that the corrosion of

CS within this temperature range is governed by the diffusion of species that have the ability to form a passive film. This is because at these temperatures, the CS undergoes active corrosion as a result of the low activation energy needed for the diffusion of potential passive species. As a result, CS exhibited uniform corrosion with an actively corroded surface and no indication of the formation of a protective film at the temperatures studied (as shown in **Figure 4. 4**).

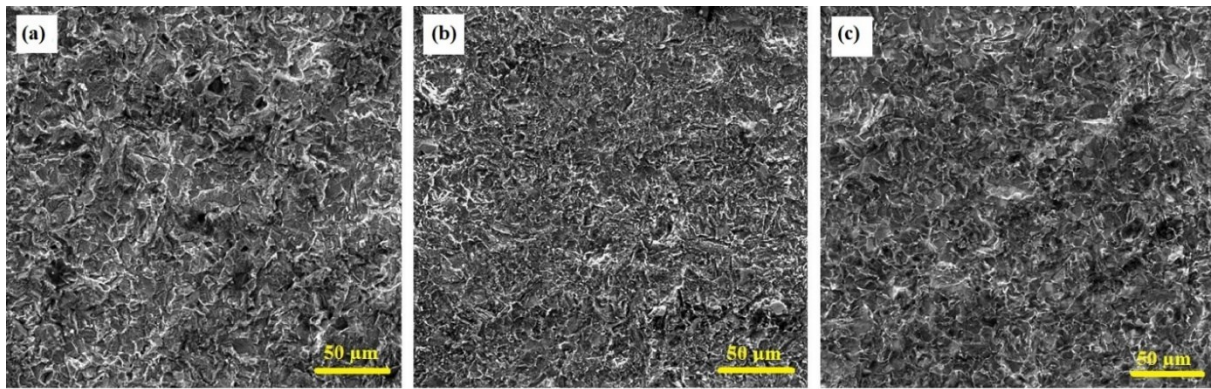


**Figure 4. 4.** Morphology of CS after 24 hours of immersion in BO. (a) at 80 °C; (b) at 150 °C; and (c) at 220 °C.

Furthermore, the corrosive nature of BO leads to the dissolution of metals, producing positive metal ions ( $M^+$ ), as indicated in **Equation 4. 2**. These ions can form highly concentrated areas during immersion experiments, leading to localized corrosion and a higher CR [61]. In order to assess the effect of elevated metal ion concentrations on metal corrosion resistance, additional immersion tests were performed for 10 hours. The tests focused on two highly susceptible metals to BO corrosion, CS and P91. These metals have low Cr content, making them more prone to

corrosion, as shown in **Table 3. 1**. In addition, research has shown that steel with high Cr content provides strong resistance to corrosion in BO environments [33].

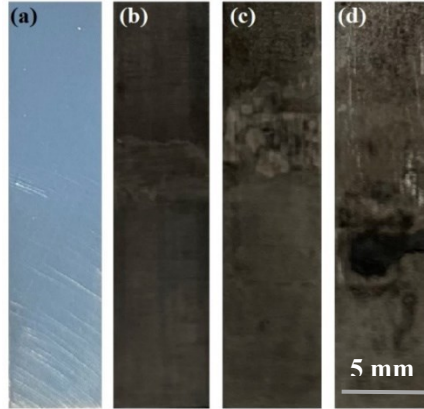


**Figure 4. 5.** Photographic images of CS: (a) before immersion; after immersion for 10 hours in BO (b) at 80 °C, (c) 150 °C, (d) and 220 °C.



After the immersion experiments, a similar behaviour was observed as in the 24-hour experiment. As the temperature increased, the coupons became darker, and their texture rougher. The middle section of the coupons, where the PTFE holder was holding them, stood out prominently, as shown in **Figure 4. 5**. Furthermore, the corroded coupons were thinner and darker than those from the 24-hour experiment, indicating greater weight loss. The CRs for CS coupons immersed with P91 coupons were 18.98, 124.76, and 147.28 mm/y at 80, 150, and 220 °C, respectively, after 10 hours of immersion (**Figure 4. 2**). In comparison to the CRs of the 24-hour experiment, the CRs for the 10-hour experiment were significantly higher. This discrepancy could

be explained by the difference in pressure experienced in both experiments, as shown in **Table 4. 2**. The pressure for the 10-hour experiment was higher at all temperatures, reaching up to >7 MPa at 220 °C. Meanwhile, the 24-hour experiment at 220 °C reached a maximum pressure of 2.3 MPa when only CS was immersed. This suggests that the presence of another source of metal ions ( $M^+$ ) increases the CR of the immersed samples.

**Table 4. 2.** Pressure registered in immersion experiments with different sets of immersed metal coupons in BO for 10 and 24 hours at 80 to 220 °C.

Temperature (°C)	Immersion time (h)	Metal Coupons	Pressure (MPa)
<b>80</b>	10	CS + P91	0
		CS	0
	24	304L + 316L	0
		P91 + HX	0.2
<b>150</b>	10	CS + P91	1.7
		CS	0.2
	24	304L + 316L	0
		P91 + HX	0.4
<b>220</b>	10	CS + P91	>7
		CS	2.3
	24	304L + 316L	0.5
		P91 + HX	2.5

Additionally, two sets of experiments were conducted to confirm the source of the elevated pressure recorded when CS and P91 were immersed together in BO. The aim was to determine whether the high pressure was due to the thermal decomposition of some of the BO constituents or primarily resulted from the reaction depicted in **Equation 4. 2**. In the first experiment, 100 mL of BO was placed in the autoclave at 150 °C for 10 hours, and no increase in pressure was recorded (0 MPa). Conversely, when adding 0.5 g of Fe<sub>2</sub>O<sub>3</sub> to the same amount of BO, the pressure reached a maximum of 0.9 MPa after the same time. In the second experiment, 100 mL of BO was also placed in the autoclave at 220 °C for 10 hours. The pressure increased slightly, reaching 0.6 MPa. However, when 0.5 g of Fe<sub>2</sub>O<sub>3</sub> was added, the pressure reached a maximum of 4 MPa after 10 hours. This suggests that the primary source of pressure increase is the anodic reaction (**Equation 4. 2**) where hydrogen (H<sub>2</sub>) is formed, leading to an increase in pressure. In the following **Chapter 5**, TGA curves will demonstrate the type of matter formed in the blank test, with just BO, when adding Fe-oxide and when immersing metal coupons.

**Table 4. 3.** Pressure registered in immersion experiments when 0.5 g of Fe<sub>2</sub>O<sub>3</sub> were added to BO for 10 hours at 150 and 220 °C.

Temperature (°C)	Immersion time (h)	Pressure (MPa)
150	0	0
	2	0.6
	4	0.7
	6	0.8
	8	0.8
	10	0.9

220

0	3
2	3.6
4	3.7
6	3.8
8	3.9
10	4.0

## 4. 2 CHROMOLY STEEL P91 IN BO

P91 was chosen for immersion testing based on its higher Cr content (~ 9 wt.%) which has been linked to higher corrosion resistance in BO compared to plain CS, as aforementioned [33]. This ferritic-martensitic steel has also been reported to exhibit good behaviour at high temperatures with high creep resistance [51]. **Figure 4. 6** shows the comparison between pre- and post-immersion images of P91, revealing that after 24 hours of immersion, the coupons darkened and roughened with a rise in temperature, similar to the results with CS.

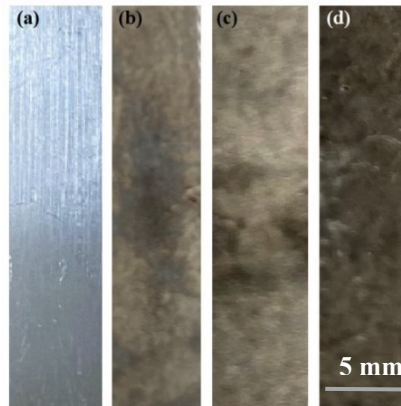


**Figure 4. 6.** Photographic images of P91: (a) before immersion; after immersion for 24 hours in BO (b) at 80 °C, (c) 150 °C, (d) and 220 °C.

After being immersed, P91 exhibited a CR of 3.497 mm/y at 80 °C for 24 hours, which is lower than the rate of 11.97 mm/y seen in CS. This aligns with prior research suggesting that metals with a higher Cr content exhibit greater resistance to corrosion. However, as temperature increased, the CR of P91 not only increased from the one presented at 80 °C but also surpassed the CR of CS at 150 and 220 °C with values of 35.91 and 73.32 mm/y, respectively. This can be observed in **Figure 4-7** that compares the CRs of P91 and CS for 24 hours. Although these rates are higher than those of CS, both steels still displayed CRs of an unacceptable magnitude for refining processes, according to **Table 4. 1**.

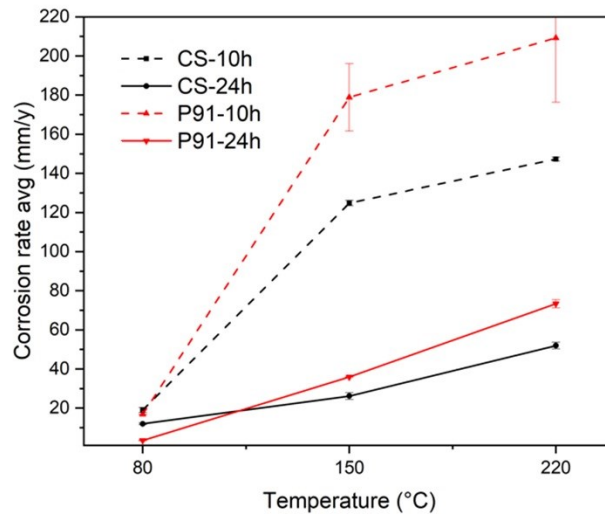


**Figure 4. 7.** The averaged corrosion rates of P91 after 10 and 24 hours of immersion in BO at 80 to 220 °C compared to those of CS.

The diffusion of potential passive species also controlled the corrosion of P91, as shown by the activation energy of 31.44 KJ/mol found in **Figure 4. 8**. Despite having a higher Cr content than CS, P91 still did not exhibit passivation within the temperature range of 80–220 °C. This is

consistent with previous research, which has found P91 to be highly susceptible to corrosion under high-temperature conditions. For instance, a study by Skobir and Spiegel [62] exposed P91 coupons to a simulated biomass combustion atmosphere and found the weight loss to be extremely high. To understand the impact of alloying elements Al, Si, and Mo on corrosion resistance, the authors developed different model alloys based on P91 with varying levels of these elements. Adding Mo alone resulted in a higher weight loss, while adding Al and Si together reduced the weight loss. The highest resistance was observed when all three elements were added together. Hence, it is possible that the P91 used in this study suffered from poor corrosion resistance at temperatures between 80–220 °C due to a lack of sufficient Al, Si, and Mo in its composition.

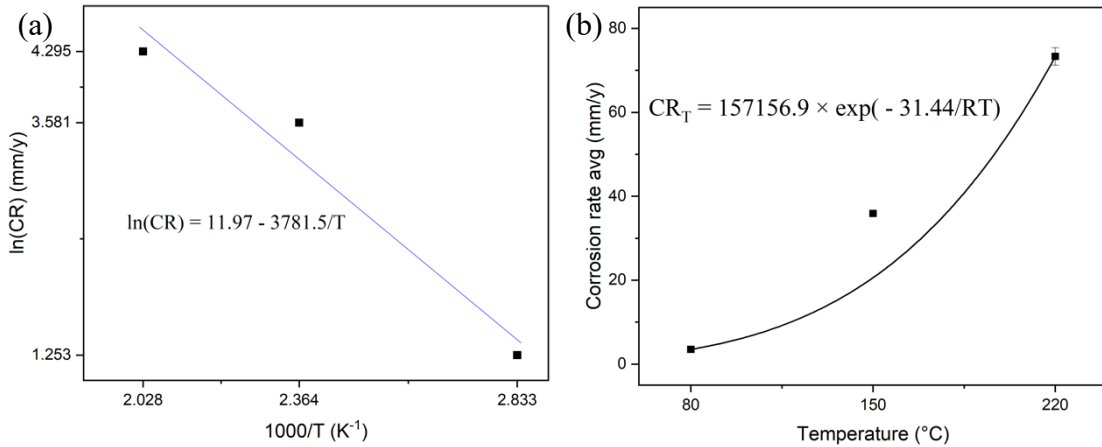


**Figure 4. 8.** Dependence of the corrosion rate of P91 on the temperature (80–220 °C) according to the Arrhenius plot for BO, (a) logarithm of the Arrhenius equation, and (b) the Arrhenius equation.

The surface morphology of post-immersion samples was analyzed using SEM. At 80 °C, some oxide deposits were observed on the surface, as shown in **Figure 4. 9 (a)**. However, these

deposits were not large enough to form a passive protective film. The slight presence of these oxides may have contributed to the lower CR compared to CS under the same conditions. As the temperature increased, the surface of P91 became uniformly corroded with no signs of a protective film, similar behaviour from CS, as shown in **Figure 4. 9 (b)(c)**. Previous studies have found that when oxide layers are formed on P91, they are high in Fe but low in Cr, which is due to the insufficient Cr content of P91 [62]. The oxides formed in a former study are also in the form of nodular deposits, similar to those seen in **Figure 4. 9 (a)** [51]. They also observed poor adhesion of the oxide scale to the substrate and cracks within the oxides at high temperatures, allowing corrosive agents to penetrate and reducing the protective effect of the oxide film [51], [62]–[64]. Which explains why P91 shows uniform corrosion at the studied temperatures of 80–220 °C.

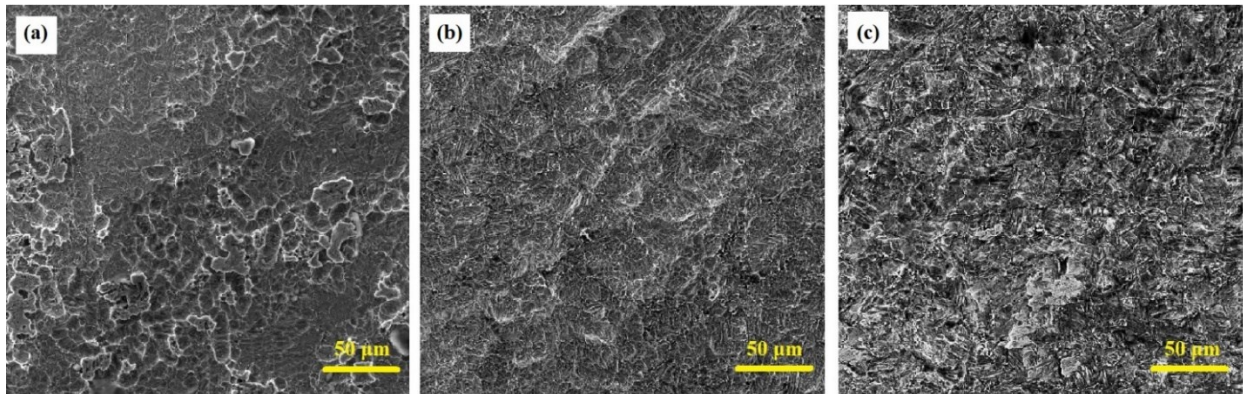


**Figure 4. 9.** Morphology of P91 after 24 hours of immersion in BO. (a) at 80 °C; (b) at 150 °C; and (c) at 220 °C.

As aforementioned, an additional immersion experiment was conducted for 10 hours with both CS and P91. The P91 coupons after immersion were found to be thinner, darker, and rougher

(Figure 4. 10) compared to the 24-hour experiment, indicating higher weight loss due to the presence of two sources of metal ions previously discussed. The observed trend was similar to the results of the 24-hour immersion experiment, where the CR for P91 after 10 hours was 16.79 mm/y, which was lower than that of CS. However, the CRs at 150 and 220 °C were higher than those of CS (178.83 and 209.22 mm/y, respectively) but still within the same order of magnitude as CS. This indicates that neither steel is suitable for the co-processing feeding lines under the studied conditions. The significant increase in pressure, as shown in Table 4. 2, and metal ion density are the main cause of higher CRs for both CS and P91 in this experiment. Previous research has established a connection between an increased pressure and the increased solubility and dissociation of passive species which could form passive protection [51]. The reason for this is that high pressure in a system exacerbates the formation of microcracks and boosts the diffusion of oxygen, thereby destabilizing and dissolving any potential passive oxides [51].

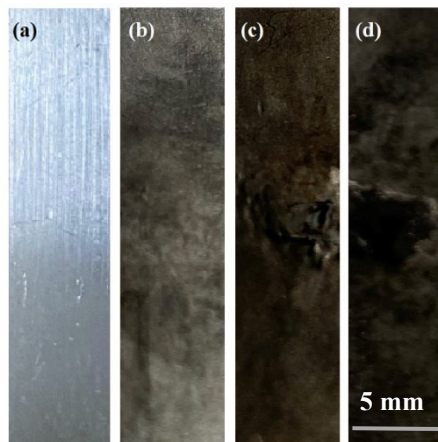


**Figure 4. 10.** Photographic images of P91: (a) before immersion; after immersion for 10 hours in BO (b) at 80 °C, (c) 150 °C, (d) and 220 °C.

### 4. 3 STAINLESS STEEL 304L IN BO

This work aims to evaluate the impact of Cr content and other alloying elements on corrosion resistance under BO. Thus, the next metal selected for immersion experiments was SS 304L due to its higher content of alloying elements compared to CS and P91 (**Table 3. 1**). As shown in **Figure 4. 11**, the SS 304L coupons did not show the brown or black coloring observed on the CS and P91 coupons after immersion. However, they underwent darkening and lost their original shine, and at 220 °C, the surface darkened further and became coarser, indicating ongoing corrosion with increasing temperature. This suggests that while SS 304L coupons may not appear as severely impacted as those of CS and P91, they are still affected by BO at 80–220 °C.

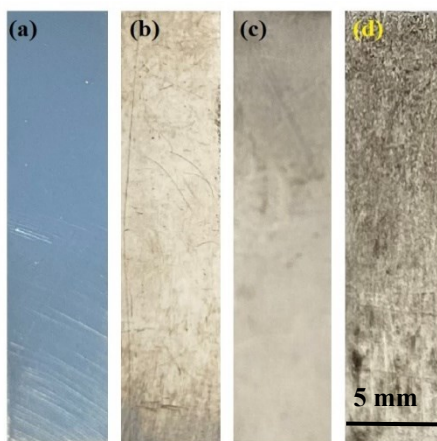


**Figure 4. 11.** Photographic images of SS 304L: (a) before immersion; after immersion for 24 hours in BO (b) at 80 °C, (c) 150 °C, (d) and 220 °C.

The same method used to determine the activation energy for CS and P91 was applied to SS 304L, yielding an activation energy of 39.30 KJ/mol, as shown in **Figure 4. 12**. Even though,

this activation energy is higher than those for CS and P91. 39.30 KJ/mol still falls in the range where the dissolution of passive scales drives the corrosion mechanism at 80–220 °C for SS 304L. The photographic images in **Figure 4. 11** and the higher activation energy support the conclusion that SS 304L is affected by BO but to a lesser extent than CS and P91. This is confirmed by the CR data in **Figure 4. 12**, with an acceptable rate of 0.29 mm/y at 80 °C, but excessive rates of 3.45 mm/y at 150 °C and 13.25 mm/y at 220 °C. Although the performance of SS 304L is not desirable at the studied temperatures, it still exhibits better CR compared to CS and P91 under BO.

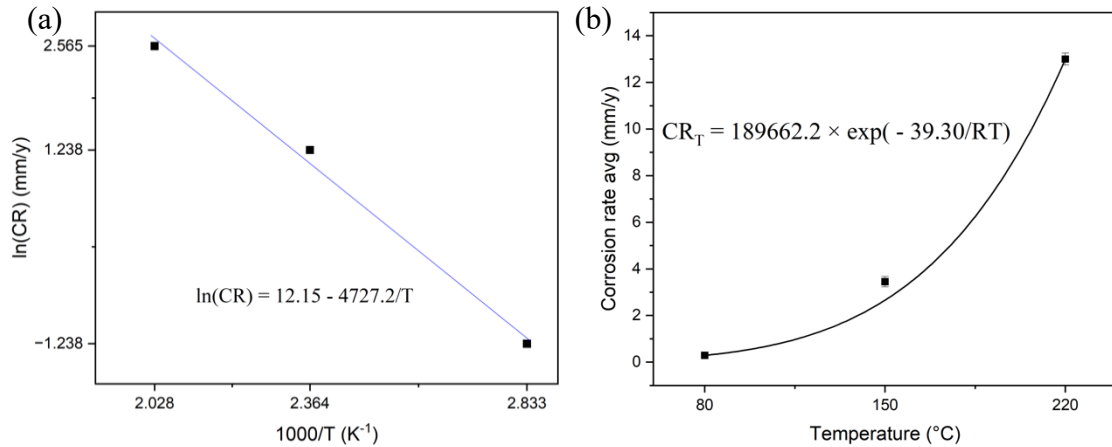


**Figure 4. 12.** Dependence of the corrosion rate of SS 304L on the temperature (80–220 °C) according to the Arrhenius plot for BO, (a) logarithm of the Arrhenius equation, and (b) the Arrhenius equation.

The superior performance of SS 304L can be attributed to its higher content of Cr, Ni, and Mo compared to P91 and CS. Previous research has shown that these elements enhance the corrosion resistance of steels [55]; regardless, Mo is not a principal alloying element on SS 304L. Former authors have proposed that Mo promotes higher Cr enrichment in the passive film due to

the synergistic effects of Cr and Mo. Also, it is well known that the addition of Ni encourages the formation of protective nickel oxides, which increases the resistance to strong acids. The relatively high Cr content in SS 304L would typically result in the formation of a passive Cr-oxide film. However, as discussed in **Chapter 2**, previous studies have observed multi-layered oxides rich in Fe rather than the expected Cr-oxides under high-temperature BO [33]. Thus, SS 304L was still affected by BO due to the higher effect of temperature on chemical dissolution in Fe-oxides compared to Cr-oxides [51], leading to insufficient protection at elevated temperatures.

The SEM analysis in **Figure 4. 13** reveals that at 80 °C, the SS 304L surface appears opaque with visible scratches from 600-grit sandpaper. As previously noted, it is believed that Fe-oxide forms a passive protective film on the SS 304L surface, and the opaque appearance could be a sign of the formation of a film. The uneven distribution of scratches suggests that the surface has been impacted by the acidity of BO. The CR of 0.29 mm/y at 80 °C also indicates that SS 304L is susceptible to BO, despite performing better than CS and P91. As temperature increases, the protective film begins to break down, exposing the grain, leading to localized intergranular corrosion at 150 °C as shown in **Figure 4. 13 (b)**. Finally, at 220 °C, the metal is actively corroded by acids within BO, dissolving the protective film created by the alloying elements (**Figure 4. 13 (c)**).

Previous studies have conducted immersion tests in BO up to 80 °C and found that SS 304L may be capable of tolerating the corrosivity of BO. However, this work demonstrates that SS 304L is not suitable for resisting the corrosion attack of raw BO at co-processing feeding

temperatures ( $>80$  °C). As previously mentioned, many components in existing FCC units are constructed with SS 304L, and one solution to mitigate risks could be to deoxygenate BO before entering the FCC unit by adding solvents (e.g., methanol) [3], [65]. However, the effect of solvents on the corrosivity of BO at FCC feeding temperatures (100–300 °C) has not yet been evaluated.

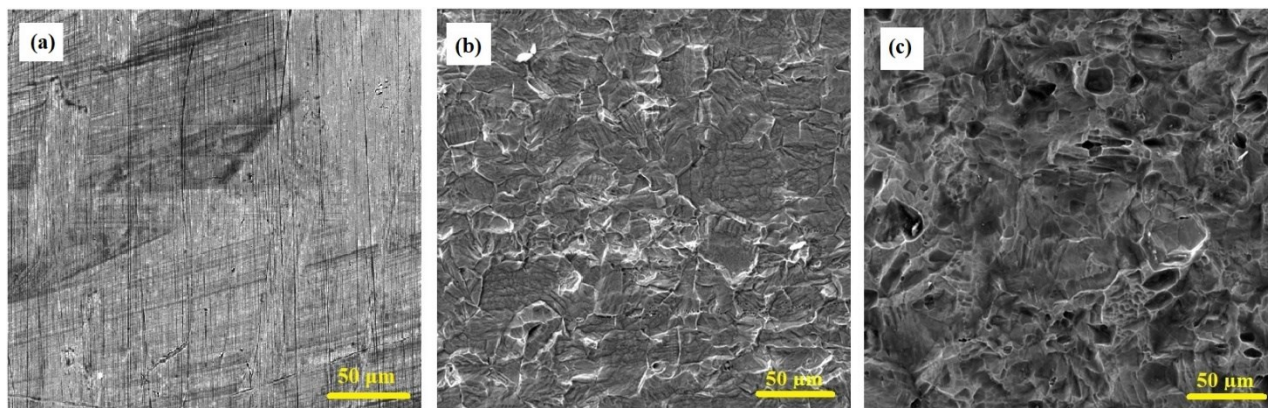


**Figure 4. 13.** Morphology of SS 304L after 24 hours of immersion in BO. (a) at 80 °C; (b) at 150 °C; and (c) at 220 °C.

#### 4. 4 STAINLESS STEEL 316L IN BO

To reduce the risks involved in co-processing BO in FCC units, another suggestion is to use a material for constructing the feeding lines, such as feeding nozzles, that has better corrosion resistance compared to SS 304L. In this regard, SS 316L was evaluated for its suitability. After conducting immersion experiments, the coupons remained gray in color, but the shine was lost, and the surface became rougher and darker at 220 °C, which might indicate active corrosion (as seen in **Figure 4. 14(d)**). These slight changes indicated in the photographic images are more promising than those for SS 304L, P91 and CS, indicating good corrosion resistance, making SS

316L a better candidate for the construction of feeding nozzles in FCC units. To further verify the corrosion resistance, X-ray diffraction (XRD) was performed to determine the nature of the protective film. The results showed that no deposited corrosion products were detected at any temperature, suggesting that the corrosion products are either too thin or amorphous, or that chemical dissolution caused by the combined action of high temperature and the acidity of BO prevented the deposition of such products. The XRD scans, which only show the substrate peaks, can be found in **Figure 4. 15**.

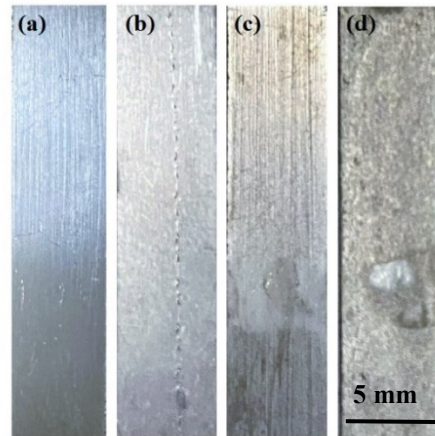


**Figure 4. 14.** Photographic images of SS 316L: (a) before immersion; after immersion in BO (b) at 80 °C, (c) 150 °C, (d) and 220 °C.

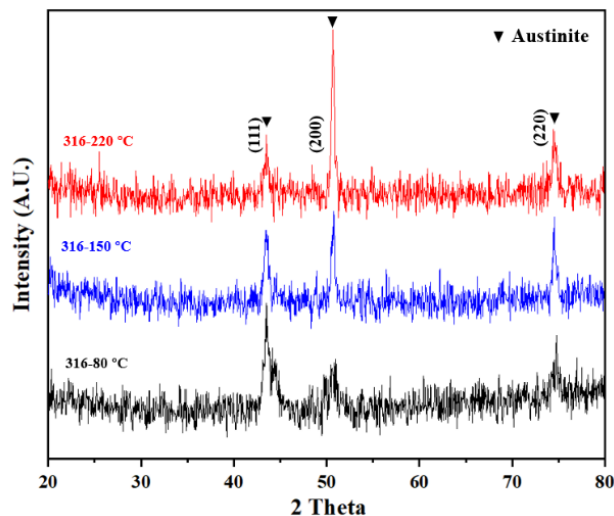


**Figure 4. 15.** XRD patterns recorded on post-immersion SS 316L coupons.

Furthermore, **Figures 4. 16** and **4. 17** display the SEM images and EDS maps of the cross-section of SS 316L post-immersion. The EDS maps in **Figure 4. 16** at temperatures of 80 °C and 150 °C clearly demonstrate the even distribution of Cr, Fe, and Ni throughout the sample, indicating that no continuous layer was formed on the surface. In contrast, the EDS maps at 220 °C reveal the formation of deposited corrosion products, as evidenced by the presence of Fe and Cr in these products along with an increase in O. A compositional mapping of selected points confirms that the metal substrate, represented by spectrum 2, primarily consists of Fe, followed by Cr and Ni, with no presence of O. Conversely, spectrums 1 and 3 exhibit a reduced amount of Fe, allowing for an increase in O, indicating the presence of corrosion products on the surface. These deposited corrosion products are mainly Fe-oxides over Cr-oxides, which explains the low corrosion resistance, as Fe-oxides are more prone to chemical dissolution at elevated temperatures [51].

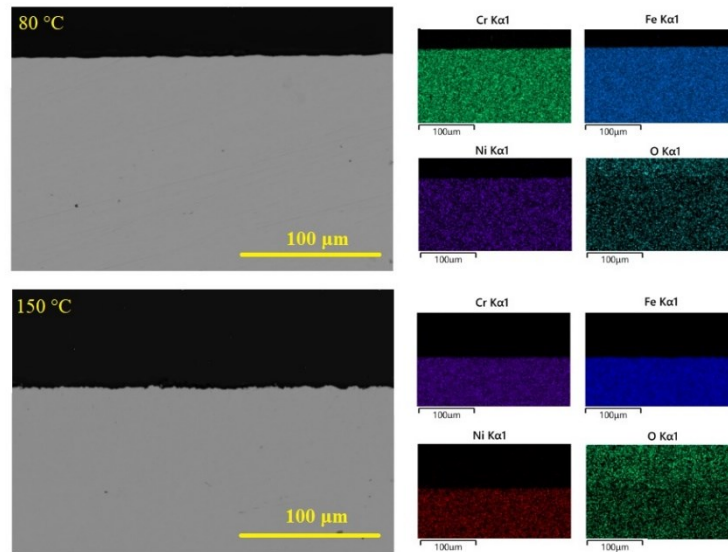


**Figure 4. 16.** SEM images and EDS maps from a cross-section of SS 316L. (a) at 80 °C; and (b) at 150 °C.

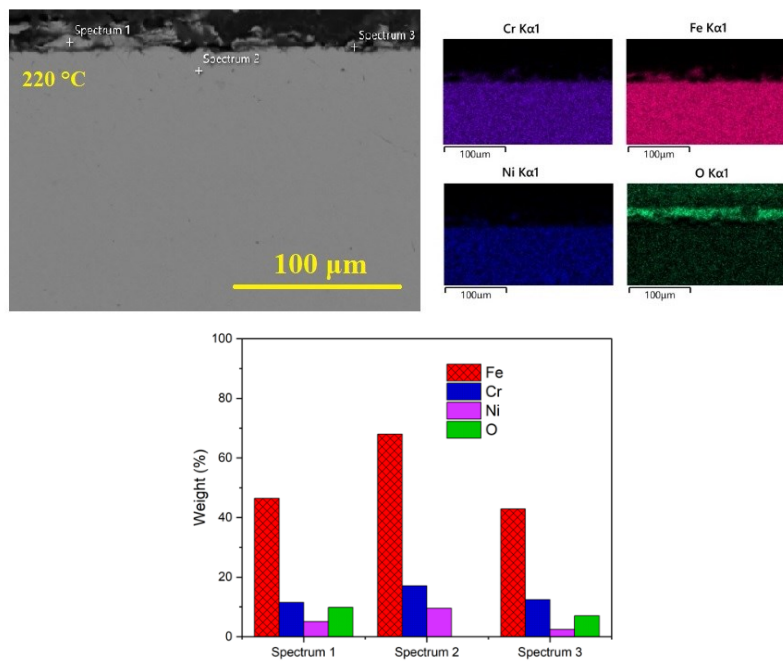


**Figure 4. 17.** SEM images and its corresponding compositional mapping by EDS from a cross-section of SS 316L at 220 °C.

The effect of temperature on the average CR of SS 316L is illustrated in **Figure 4. 18**. At 80 °C, the CR was recorded at 0.06 mm/y, consistent with previous findings of less than 0.1 mm/y [3]. As the temperature increased in increments of 70 °C, the CR increased by one order of magnitude, reaching 0.62 mm/y and 1.77 mm/y at 150 °C and 220 °C, respectively. These results highlight the influence of temperature on the corrosion resistance of SS 316L, in agreement with previous studies that reported a CR below 0.01 mm/y at 50 °C [3], [29]. **Figure 4. 18** also compares the corrosion resistance of SS 316L with that of SS 304L. It was reported above that SS 304L showed acceptable corrosion resistance of 0.29 mm/y at 80 °C for 24 hours, however excessive corrosion was observed at 150 °C (3.68 mm/y) and 220 °C (13.25 mm/y). While metals with higher Cr content typically have higher corrosion resistance against BO [33], the comparison of Cr content in SS 304L (18.28 wt%) and SS 316L (16.57 wt%) reveals that SS 304L exhibited higher susceptibility to corrosion in BO environments. However, when considering other elements that contribute to corrosion resistance in steels, such as Ni and Mo [55], it is noted that SS 316L has higher contents of both Ni and Mo compared to SS 304L. Thus, the corrosion resistance of the metals against BO constituents is not solely dependent on the addition of Cr, but also on the presence of alloying elements Ni and Mo.

As aforementioned, the classification of CRs is subjective, and **Table 4. 1** demonstrates that NACE—SP0775-2018 is more restrictive than Bradford (2001) for oil production systems [56], [57]. Hence, according to NACE—SP0775-2018, the CRs of SS 316L were moderate at 80 °C (0.06 mm/y) and severe at 150 °C and 220 °C (0.62 and 1.77 mm/y). **Figure 4. 18** clearly indicates that 80 °C serves as a turning point for SS 316L, transitioning from high corrosion resistance (i.e., low CR < 0.01 mm/y) (presented as a \*) to low corrosion resistance (i.e., active CR > 0.1 mm/y)

in BO. This study identifies 80 °C as the critical temperature ( $T_{cr}$ ) for active corrosion in BO for SS 316L. To further examine the activation of corrosion in SS 316L, an Arrhenius plot is presented in **Figure 4. 19**.

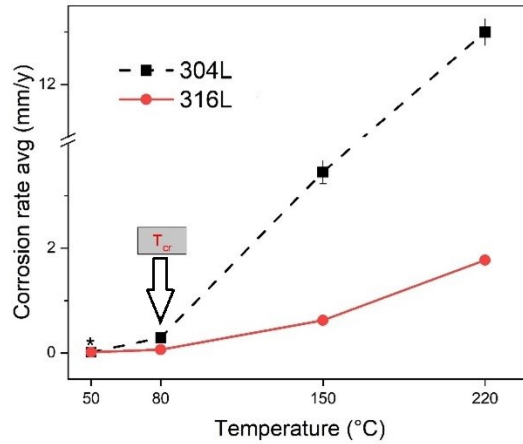


**Figure 4. 18.** Effect of temperature on the corrosion rate of SS 316L compared to commonly used structural SS 304L.

Similar to CS, P91, and SS 304L, the CR of SS 316L increased with temperature in an exponential manner, as depicted in **Figure 4. 19 (b)**. The molar activation energy for the corrosion of SS 316L in BO, between 80 and 220 °C, was calculated to be 34.98 KJ/mol. As SS 304L, the activation energy of SS 316L was higher than those of CS and P91. However, between 80 and 220 °C, the corrosion of SS 316L was primarily driven by the diffusion of passive species from its protective film, causing the film to eventually deteriorate. An excellent example of a well-preserved passivation system is the duplex SS 2205 under condensed-phase corrosion experiments up to 150 °C, conducted by Li et al. [58]. They recorded a CR of just below 0.0020 mm/y at 150 °C, with a molar activation energy of 50.28 KJ/mol, demonstrating the ability of the oxide scales

to withstand that environment. The higher activation energy of duplex SS 2205 can be attributed to its composition, which contains higher Cr (22.54 wt.%) and Mo (3.03 wt.%) than SS 316L.

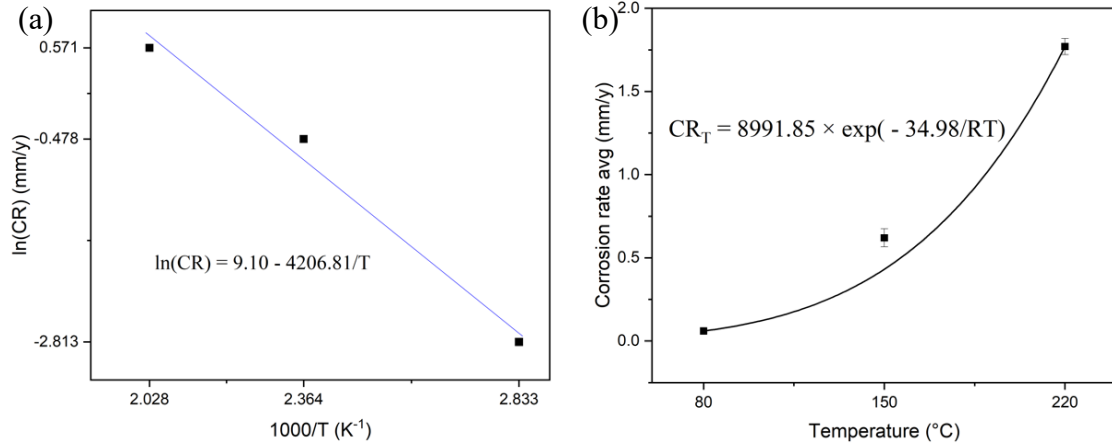


**Figure 4. 19.** Dependence of the corrosion rate of SS 316L on the temperature (80–220 °C) according to the Arrhenius plot for BO, (a) logarithm of the Arrhenius equation, and (b) the Arrhenius equation.

The SEM micrographs in **Figure 4. 20** present the top-view of the corroded surface of SS 316L at the studied temperatures. The grains are exposed as a sign that BO constituents mainly act through the grain boundaries. This observation is also noted by Brady et al. [33] and Wang et al. [3]. The intergranular corrosion in the grain boundaries of SS 316L is a result of selective leaching, with previous reports suggesting the leaching of Cr and Ni from this type of SS [66]. As temperature rises, the severity of localized intergranular corrosion intensifies, as evidenced in **Figure 4. 20** (c). This confirms that elevated temperatures negatively impact the corrosion resistance of SS 316L. Brady et al. [33] found that the selective leaching of Cr was due to the formation of Cr-sulfides in high sulfur co-FCC environments. They also found that SS with higher

Mn content did not show intergranular attack, proposing that Mn-sulfides form over Cr-sulfides, leaving more Cr available for metal passivation [33], [67]. It is hypothesized that Cr moves from the bulk metal to the surface in the form of Cr-oxides, creating a passive protective barrier [68]. This barrier prevents the rapid diffusion of O from highly-oxygenated BO molecules towards the base metal [68]. However, as temperature rises, the acidity within BO leads to more severe selective corrosion at the grain boundaries, leading to the leaching of Cr and the destruction of the passive protection [67]. This also explains why the oxides identified in **Figure 4. 17** are Fe-oxides instead of Cr-oxides.

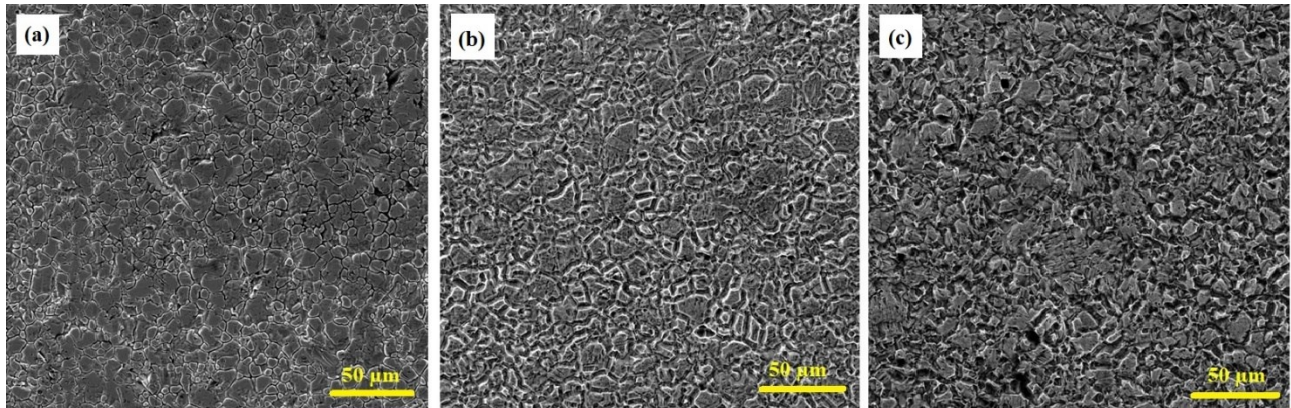


**Figure 4. 20.** Morphology of SS 316L after 24 hours of immersion in BO. (a) at 80 °C; (b) at 150 °C; and (c) at 220 °C.

#### 4. 5 NICKEL-BASED ALLOY HX IN BO

Finally, we studied a nickel-based alloy known as HX. Despite not being widely used as a structural metal in petroleum refineries, it was selected for its higher content of Cr, Mo, and of course, Ni. The HX was used as a reference to compare with the lower grade alloys CS, P91, and

the SSs 304L and 316L. The photographic images in **Figure 4. 21** reveal that the HX coupons were not impacted by BO at the studied temperatures. This is in contrast to the images of SS 316L in **Figure 4. 14**, which showed the highest resistance among the previous four metals studied. The results indicate that the combined effect of BO corrosivity and temperature did not harm the HX due to its high corrosion resistance.

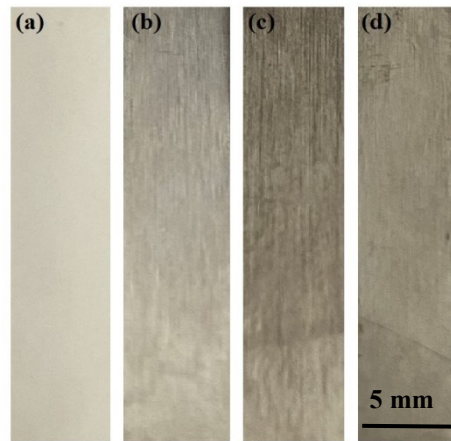


**Figure 4. 21.** Photographic images of HX: (a) before immersion; after immersion in BO (b) at 80 °C, (c) 150 °C, (d) and 220 °C.

The results of the study on the effect of temperature on the CR of HX, as shown in **Figure 4. 22**, demonstrate the superior corrosion resistance of the HX. At all temperatures studied, ranging from 80–220 °C, the CR of HX was “moderate”, according to NACE-SP0775-2018, and "good" per Bradford (2001) criteria, with a CR < 0.05 mm/y. Further comparisons of the corroded coupons from the five different metals after exposure at a representative temperature of 150 °C, as depicted in **Figure 4. 23**, reveal that the surface of the corroded HX sample is smoother and unaffected compared to the rough and corroded appearance of the surfaces of CS, P91, and SS 304L samples, which likely lack a passive protective film. The absence of deposited corrosion products at this

temperature, as indicated by the SEM micrographs, may be due to chemical dissolution, as discussed above.

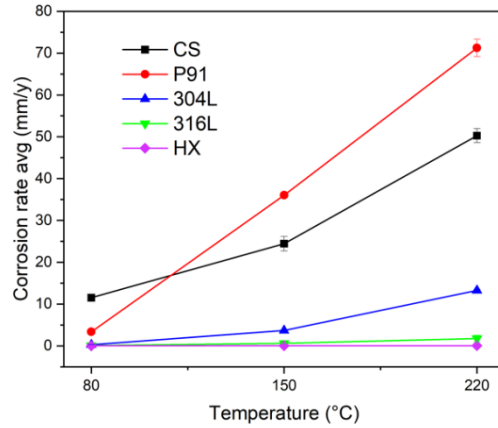


**Figure 4. 22.** The averaged corrosion rates of the five metals studied after 24 hours of immersion in BO at 80 to 220 °C.

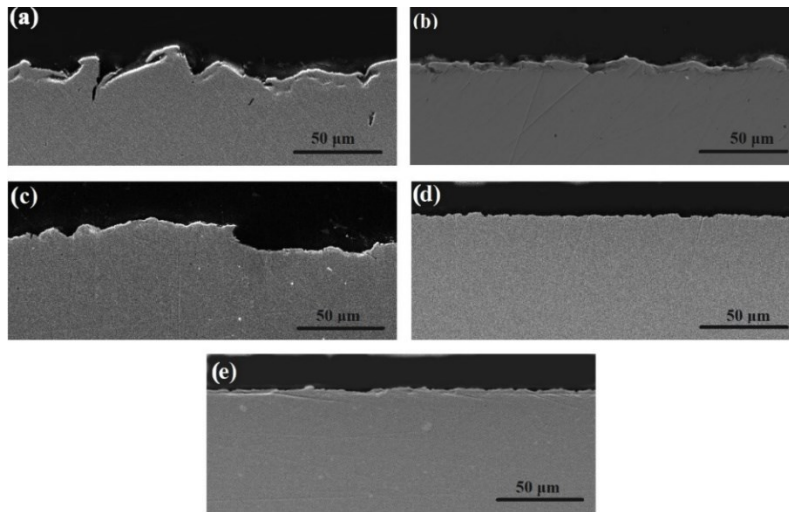


**Figure 4. 23.** SEM micrographs of the cross-sections of corroded samples at 150 °C. (a) CS; (b) P91; (c) SS 304L; (d) SS 316L; and (e) HX.

Using a similar process as that used to calculate the activation energy of the previously studied metals, the activation energy of HX in BO at temperatures between 80–220 °C was determined to be 2.31 kJ/mol (**Figure 4. 24**), which is outside the range of 10–45 kJ/mol discussed earlier. Thus, the diffusion of passive species does not occur due to the high corrosion resistance of HX. The weight loss was nearly negligible, indicating CRs of 0.037 mm/y, 0.031 mm/y, and 0.047 mm/y at 80, 150, and 220 °C, respectively. Although the differences between the two coupons immersed at each temperature resulted in high errors, the errors are negligible in absolute terms. As the CRs do not vary much with temperature, the activation energy is not an adequate method to determine the corrosion behavior of HX, as the metal can be considered unaffected.

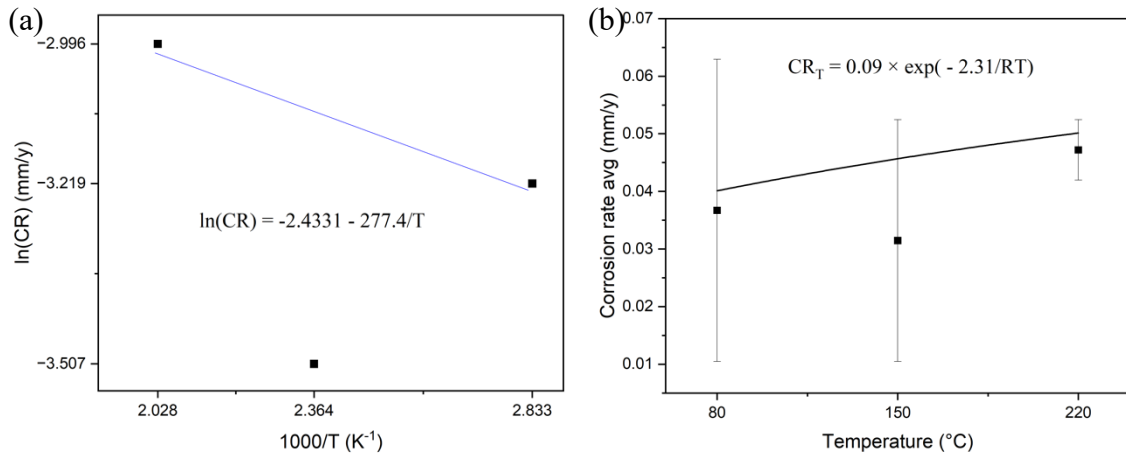


**Figure 4. 24.** Dependence of the corrosion rate of HX on the temperature (80–220 °C) according to the Arrhenius plot for BO, (a) logarithm of the Arrhenius equation, and (b) the Arrhenius equation.

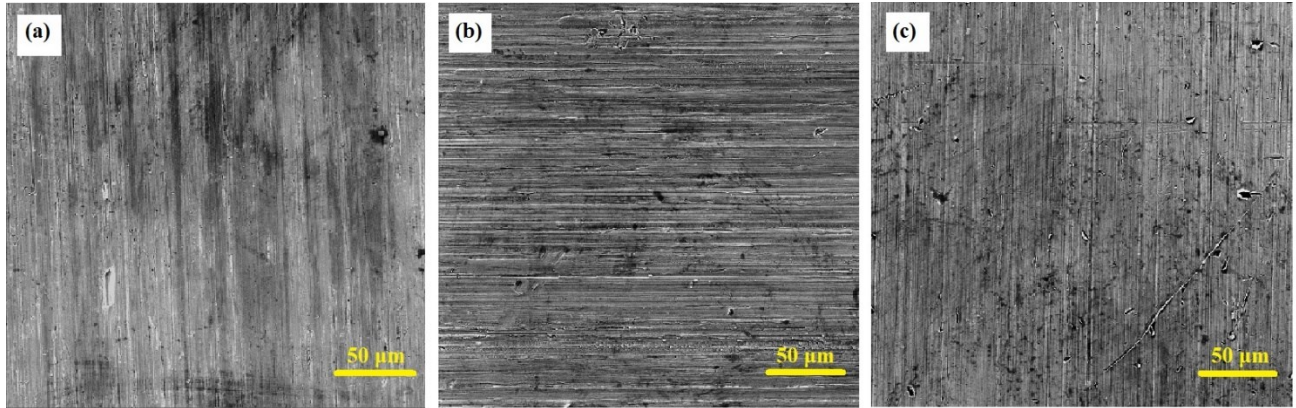


**Figure 4. 25.** Morphology of HX after 24 hours of immersion in BO. (a) at 80 °C; (b) at 150 °C; and (c) at 220 °C.

As depicted in **Figure 4. 25**, the SEM micrographs confirm that the BO used in the temperature range of 80–220 °C did not corrode the surface of HX. Notably, the scratches from the 600-grit SiC sandpaper used during the coupon preparation for immersion experiments were still visible on the surface. The surface of HX remained unaffected due to its high content of Cr (21.5 wt.%), Ni (>45 wt.%), and Mo (8.38 wt.%).

# CHAPTER 5 THERMOSTABILITY OF PYROLYSIS OIL UP TO 220 °C

This chapter discusses the outcomes of aging experiments conducted on BO to explore the variations in its physical and chemical characteristics caused by its thermal instability. The experiments were conducted at co-FCC feeding temperatures of 80, 150, and 220 °C for different durations, excluding the presence of metals. The findings of the experiments showed that BO separated into liquid and solid phases after aging. Furthermore, this section also analyzes the BO samples used in some immersion experiments with metals to examine the impact of immersed samples. Part of this Chapter has been published and presented as *H. Pedraza, H. Wang, X. Han, Y. Zeng and J. Liu, “Investigating the thermal stability and corrosivity of biocrude oil at FCC feeding temperatures for co-processing applications” AMPP 2023* and *H. Pedraza, H. Wang, X. Han, Y. Zeng and J. Liu, “Corrosion and Aging Risk Assessment of the co-FCC Feed Injection System” Biomass and Bioenergy 2023*.

## 5.1 AGING EXPERIMENTS OF BO AT 80 °C

**Table 5. 1** serves as a comprehensive summary of the results obtained from the aging experiments carried out at 80 °C. Interestingly, no phase separation was observed when the aging experiment was conducted at 80 °C for 24 hours. However, the viscosity and density of the entire BO sample did exhibit a slight increase, with values of 360 cP and 1.22 g/mL, respectively, compared to the unaged BO, with values of 189.3 cP and 1.21 g/mL, as shown in **Table 3. 2**. These

results provide crucial information regarding the thermal stability of BO at a lower aging temperature and time. As highlighted in the introductory chapter, TGA is a powerful tool for analyzing changes in the physical and chemical properties of BO when phase separation occurs during aging. TG curves provide the onset and completion temperatures of thermal reactions, weight loss during a reaction, and the rate of weight change. The resulting DTG curve is obtained by calculating the first derivative of the TG curve, which depicts the rate of mass loss against temperature.

**Table 5. 1.** Phase separation in aging experiments at 80 °C for 24, 96, and 168 hours. (a) film; (b) top+ bottom (liquid phase).

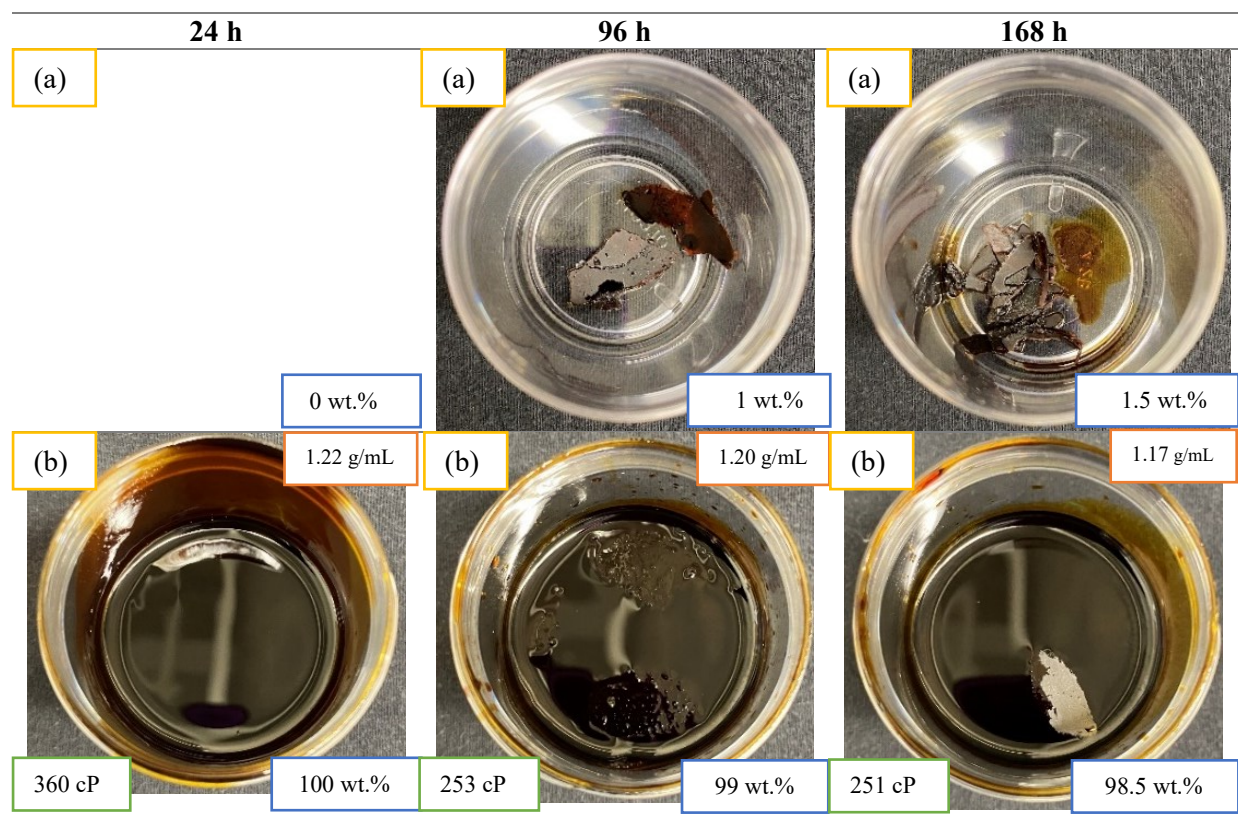


**Figure 5. 1** provides a graphical representation of the TG and DTG curves obtained for BO/stock. The DTG curve illustrates that the highest mass loss occurs near 100 °C, indicating the presence of high-water content in BO, which leads to mass loss near this temperature. To confirm the absence of phase separation at 80 °C for 24 hours, TGA was performed on samples from the top and bottom of the BO to compare their TG profile with that of unaged BO. The TG curves for the top and bottom samples were found to be similar to the TG curve of unaged BO, indicating that no phase separation had occurred, as shown in **Figure 5. 2**. The slight changes in viscosity and density were not necessarily an indication of phase separation in BO.

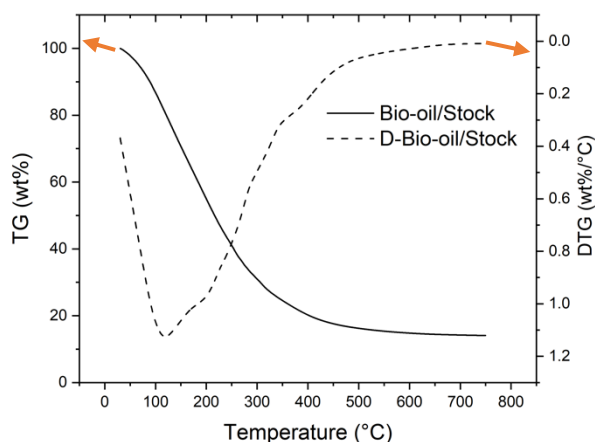


**Figure 5. 1.** TG and DTG curve of BO/Stock.

In contrast, phase separation was observed at 80 °C for the rest of the time slots, as detailed in **Table 5. 1**. At 80 °C, two phases were formed after 96 and 168 hours of aging, with a solid-like cluster (film) visible on the summit of the sample and a viscous liquid present in the rest of the sample. A schematic representation of this phenomenon is shown in **Figure 5. 3**. After carefully separating the film from the rest of the BO, to make sure the liquid was a single phase; one sample was

collected from the top of the liquid and one from the bottom. Both top and bottom samples exhibited similar viscosity and density to the aging experiment conducted at 80 °C for 24 hours.

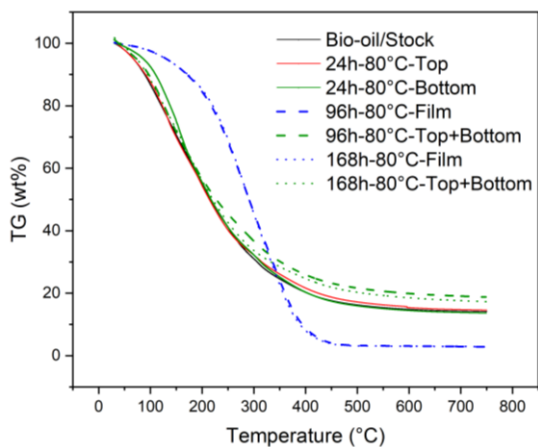


**Figure 5. 2.** Influence of aging time in the TG curves of phase separation at 80 °C.

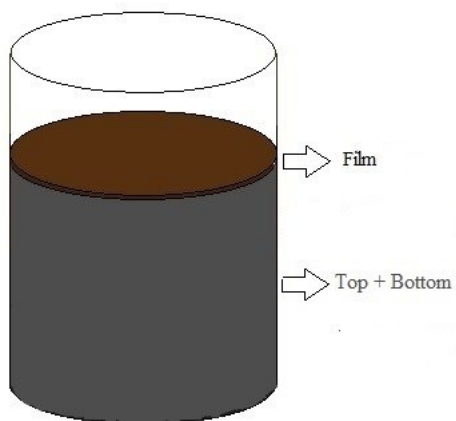


**Figure 5. 3.** Schematic of phase separation in BO aging experiments at 80 °C.

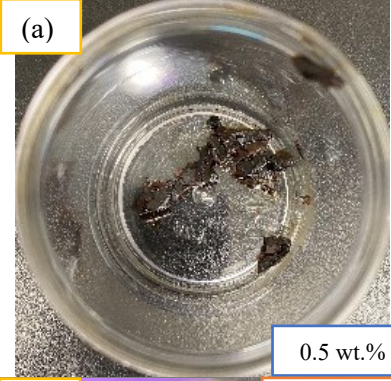
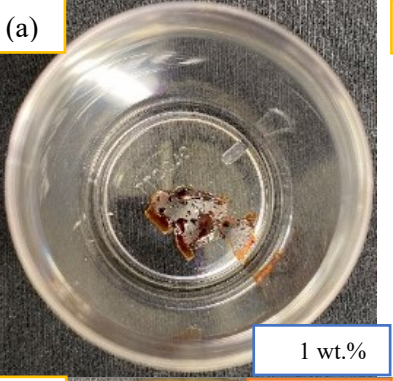
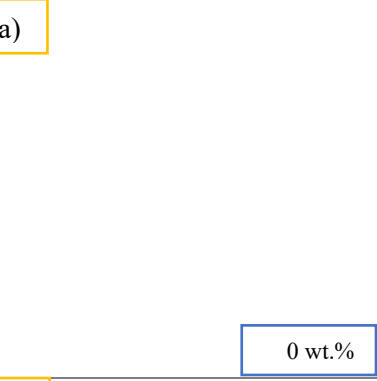
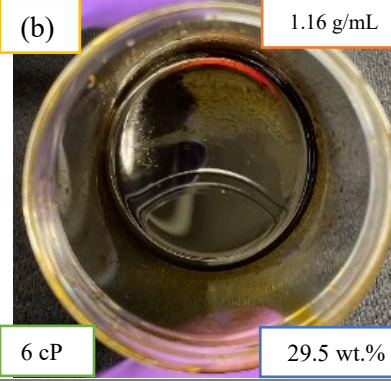
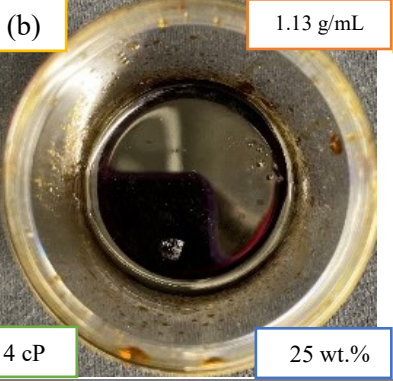
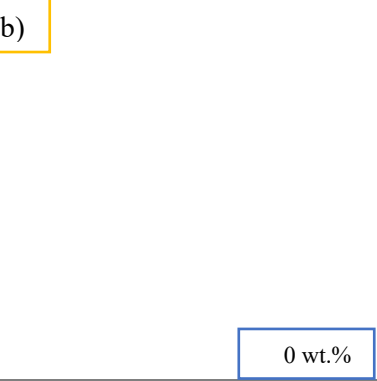
Consequently, TGA was performed only on the bottom sample for 96 and 168 hours, which revealed a slightly upper right shift in the TG curve as the aging time increased. In addition, the content of the film increased over time at the expense of the liquid content. The viscosity in the liquid phase decreased when the film was formed at 96 and 168 hours (250 cP) compared to the 24-hour experiment, where no film was present. This decrease in viscosity is indicative of the formation of organic compounds with longer chains in the film, which was confirmed by TGA. The TGA profiles for both films at 96 and 168 hours exhibited a rapid weight loss between 200 and 400 °C. In contrast, the unaged BO and the liquid phase at each aging time began losing weight at 100 °C, which is attributable to the high-water content in the BO [3], [19].

## 5. 2 AGING EXPERIMENTS OF BO AT 150 °C

Furthermore, **Table 5. 2** presents the findings of aging experiments conducted for 24, 96, and 168 hours at 150 °C. The experimental observations are also depicted in **Figure 5. 4**, which shows a film on the surface of the sample, a liquid layer at the top, and a solid layer at the bottom. The film formed at 24 and 96 hours was 0.5 and 1 wt.%, respectively; no film formation was observed at 168 hours. Additionally, the amount of the top liquid layer also decreased from 29.5 wt.% to 25 wt.% from 24 to 96 hours, and no liquid layer was formed at 168 hours. The liquid phase that formed at 24 hours had a density of 1.16 g/mL and a viscosity of 6 cP, while the liquid phase that formed at 96 hours not only had a lower amount but also a lower density and viscosity of 1.13 g/mL and 4 cP. After 168 hours of aging, only a solid phase was observed.

The bottom solid-like layer increased with time, accounting for 100 wt.% of the BO sample after 168 hours. This suggests that over time, some components in the liquid phase reacted and migrated to the solid phase, e.g., by polymerization. At 168 hours, the solid phase made up the whole sample since there was enough time to convert the wide range of molecules into long-chain compounds. Due to the solid state of the bottom layer and film, the viscosity and density measurements were not carried out.

**Table 5. 2.** Phase separation in aging experiments at 150 °C for 24, 96, and 168 hours. (a) film; (b) top layer (liquid phase); and (c) bottom layer (solid phase).

	24 h	96 h	168 h
(a)			
	0.5 wt.%	1 wt.%	0 wt.%
(b)			
	1.16 g/mL	1.13 g/mL	0 wt.%
	6 cP	4 cP	0 wt.%
	29.5 wt.%	25 wt.%	0 wt.%

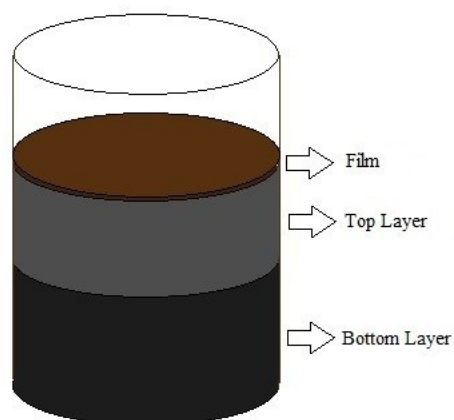
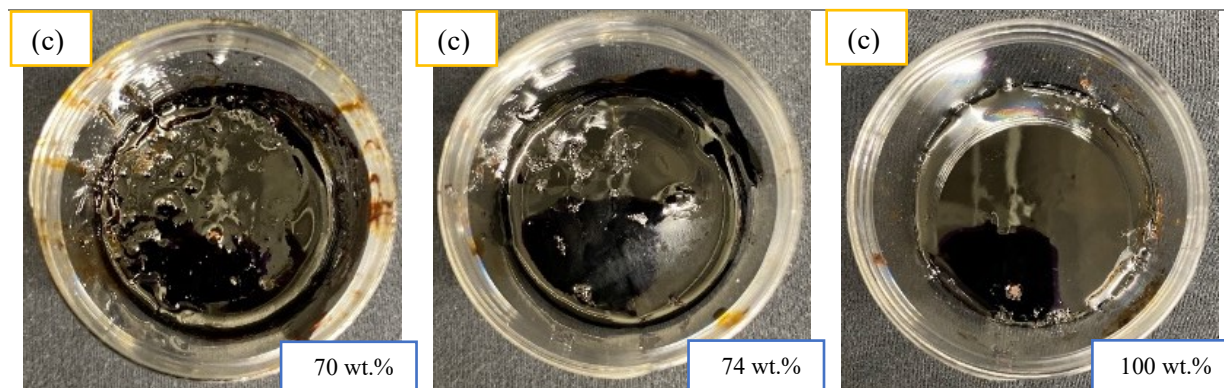


**Figure 5. 4.** Schematic of phase separation in BO aging experiments at 150 °C.

TGA was utilized to investigate the thermal decomposition of the samples and their respective formed phases. The results obtained from TGA, in conjunction with the viscosity and density data, were utilized to identify the type of organic matter present in the phases. For example, when comparing the aforementioned TG profile, for 24 hours of the top layer and the BO/stock in **Figure 5. 5**, it is observed that the TG curve for the top layer shifts to the lower left, indicating that this layer is composed of the light fractions of BO.

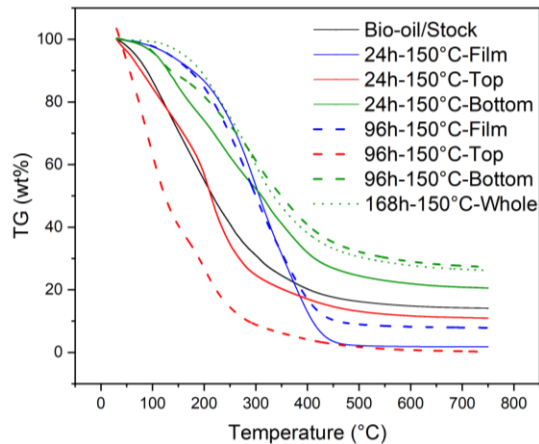


**Figure 5. 5.** Influence of aging time in the TG curves of phase separation at 150 °C.

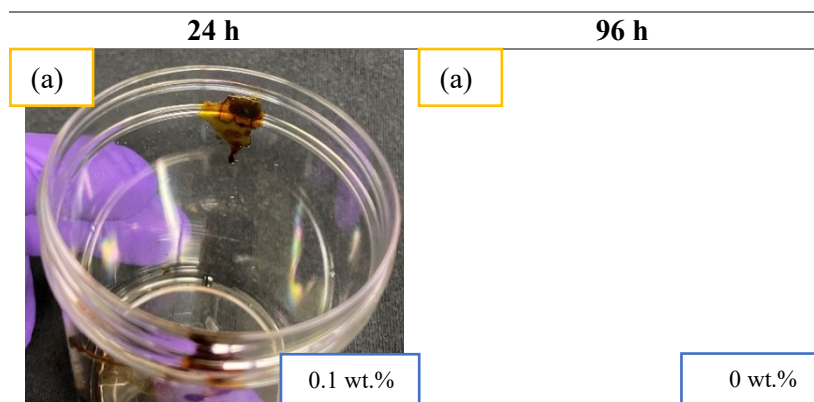
In contrast, the TG curves for the film and the bottom layer shift upper right, which indicates the presence of heavier organic matter due to the reaction among the reactive functional groups, resulting in long-chain hydrocarbons. The TG curve for the film formed at 96 hours exhibited a similar behavior to that formed at 24 hours, indicating that the films developed at different times consist of a similar type of heavy organic matter. The time influence of BO aging is clearly understood when comparing the TG curve for the liquid and solid phases at 24 and 96 hours. The TG curve for the liquid phase, at 96 hours, shifts to the lower left compared to the one at 24 hours. As previously mentioned, a lower-left curve confirms the presence of lighter fractions. Then, the viscosity (4 cP), density (1.13 g/mL), and TG curve validate that the top layer comprises lighter BO fractions as aging time increases (96 hours), as indicated in **Figure 5. 5**. Yet, the liquid phase disappeared once the light fractions are given enough time to transform into heavier organic matter. The bottom layer then absorbed the heavier organic matter, increasing its content. Compared to the TG curve of the solid phase at 24 hours, the TG curves at 96 and 168 hours shift to the upper

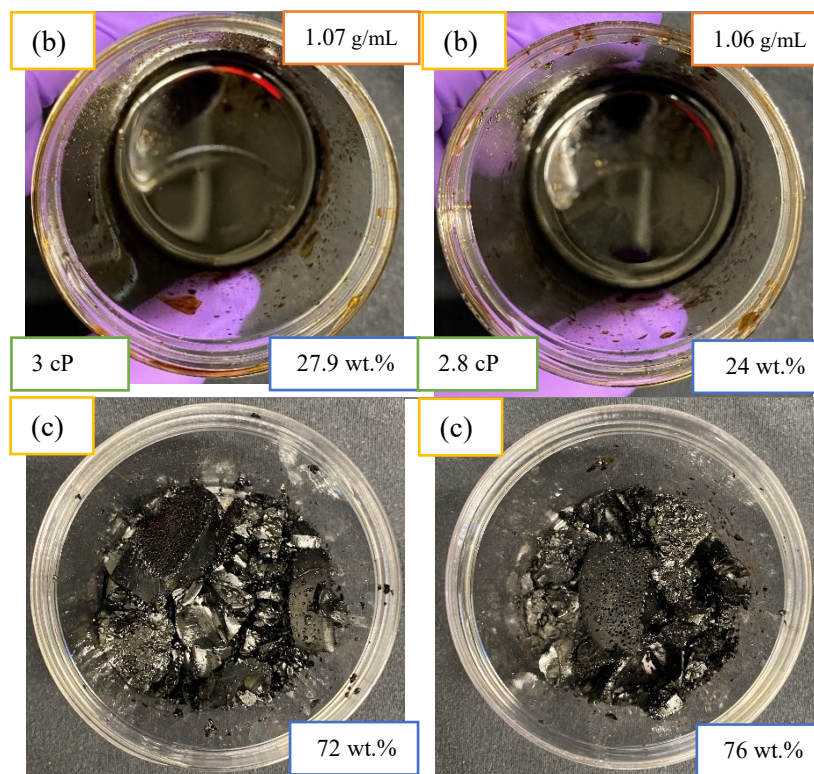
right, and the TG curve at 168 hours was above all the others. Hence, longer aging times promoted the formation of larger and heavier organic compounds.

### 5.3 AGING EXPERIMENTS OF BO AT 220 °C

Phase separation was also observed at 220 °C (**Table 5. 3**). At 24 hours three phases were observed, similar to those observed at 80 and 150 °C: a film in the summit, a non-viscous liquid in the top, and a char-like solid in the bottom (**Figure 5. 6**). The film formed at 220 °C for 24 hours was significantly thinner than those formed at 80 and 150 °C. However, similar organic matter was formed in this phase since TG curves are similar in **Figure 5. 7**. On the other hand, the liquid phase formed at the top had a significant low viscosity (3 cP) and density (1.07 g /mL), which indicates that light fractions and the water content migrate to this phase. This is supported due to its TG curve shifts lower left in **Figure 5. 7**. The char-like solid phase showed an aggressive shift to the upper right indicating that the reactive functional groups within BO interact through different reactions, e.g., polymerization, producing heavier organic matter, as aforementioned [16], [69].

**Table 5. 3.** Phase separation in aging experiments at 220 °C for 24, 96, and 168 hours. (a) film; (b) top layer (liquid phase); and (c) bottom layer (solid phase).





As indicated in **Table 5. 3** and **Figure 5. 7** similar behavior was observed at 220 °C for 96 hours, except that the thin film was not formed at 96 hours, but instead the solid phase increased at spend of liquid content. TG curves for the top and bottom for 96 hours shifted slightly lower-left and upper-right, respectively, compared to those for 24 hours. The former indicates that time promotes aging reactions, but slightly. Aging experiments were not performed at 220 °C for 168 hours due to previously it was observed 100 wt.% of solid content at 150 °C for the same time. Thus, is predicted that the solid phase at 220 °C will also cover the whole sample.

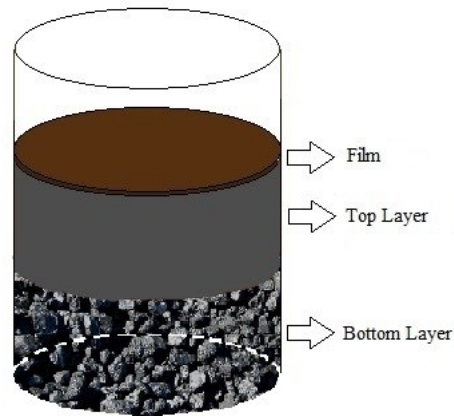


**Figure 5. 6.** Schematic of phase separation in BO aging experiments at 220 °C.

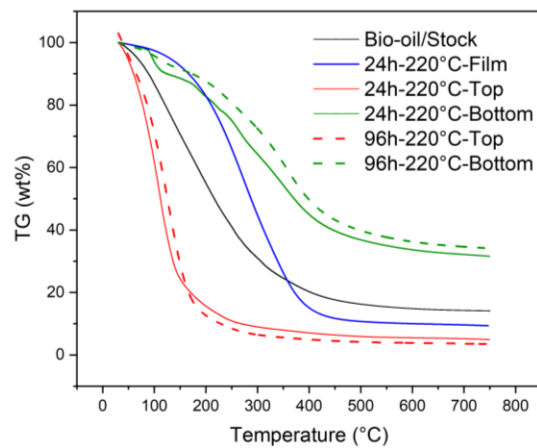


**Figure 5. 7.** Influence of aging time in the TG curves of phase separation at 220 °C.

## 5. 4 SUMMARY OF INFLUENCE OF AGING TEMPERATURE ON PHASE SEPARATION

The highlights of the aging experiments, including all phases observed at various temperatures and times and their corresponding properties, are summarized in **Table 5. 4**. As previously noted,

the aging reactions and phase separation are slightly promoted by aging time. By comparing **Figures 5. 2, 5. 5, and 5. 7** with **Figure 5. 8**, it is evident that both aging time and temperature promote aging reactions. However, the effect of temperature is more severe than that of time, as evidenced by the aggressive shift of the top and bottom curves at 220 °C away from the unaged BO and those at 80 and 150 °C for 24 and 96 hours. Therefore, **Figure 5. 8** clearly demonstrates that temperature has a more negative impact on solid phase production than time. The resulting undesired char production can lead to various issues during co-processing, such as plugging and pressure drops [5].

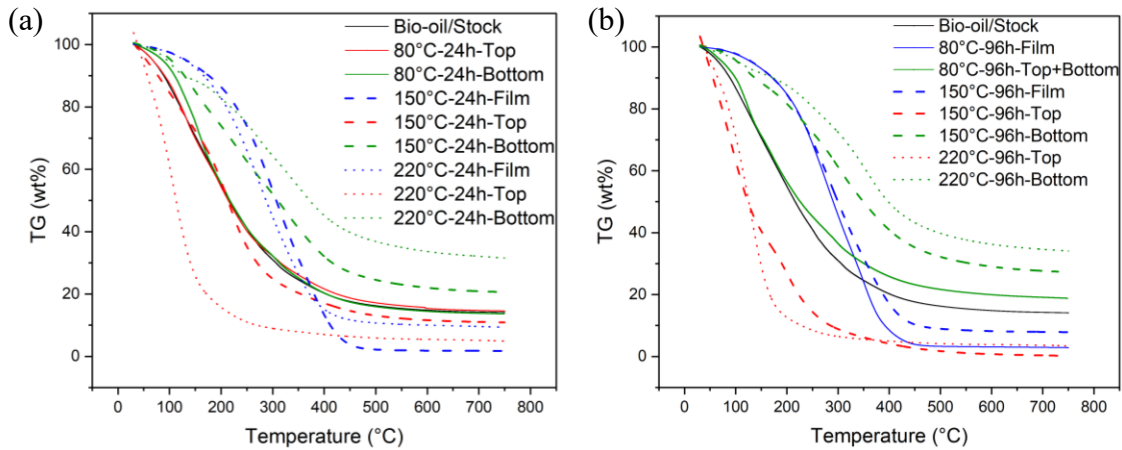


**Figure 5. 8.** Influence of temperature in phase separation. (a) TG curves in aging experiments for 24 hours, and (b) TG curves in aging experiments for 96 hours.

**Table 5. 4.** Summary of phase separation from aging experiments at 80, 150 and 220 °C for 24, 96, and 168 hours.

Temperature (°C)	Time (h)	Phases formed	Viscosity (cP)	Density (g/mL)	Weight fraction (wt.%)
80	24	-	-	-	0
		Liquid	360	1.22	100
		-	-	-	0
	96	Film	-	-	1
		Liquid	253	1.2	99
		-	-	-	0
		Film	-	-	1.5
	168	Liquid	251	1.17	98.5
		-	-	-	0
		Film	-	-	0.5
150	24	Liquid	6	1.16	29.5
		Solid	-	-	70
		Film	-	-	1
	96	Liquid	4	1.13	25
		Solid	-	-	74
		-	-	-	0
	168	-	-	-	0
		Solid	-	-	100
		Film	-	-	0.1
	220	24	Liquid	3	1.07
Solid			-	-	72
-			-	-	0
96		Liquid	2.8	1.06	24
		Solid	-	-	76
		-	-	-	0

## 5.5 SOLID CONTENT IN AGING EXPERIMENTS

**Figure 5. 9** depicts the solid content variation as a function of aging time at different temperatures of 80, 150, and 220 °C. This analysis considers both the film formed on the summit and the solid phase formed at the bottom as part of the solid content. To determine the critical time ( $t_{cr}$ ) for solid formation, additional aging experiments were conducted at each temperature, specifically for times shorter than 24 hours. The  $t_{cr}$  is defined as the time when the solid content begins to increase significantly. At a temperature of 80 °C, the first solids began to form after 24 hours. In contrast, at 150 °C, the  $t_{cr}$  was found to be 14 hours, indicating a faster polymerization process at higher temperatures. At 220 °C, the  $t_{cr}$  was close to zero hours, suggesting that at this temperature, some energy has already been gained by the pre-heating process, and solid formation can be expected as soon as the temperature reaches 220 °C.

In addition to the critical temperature for active corrosion, which was discussed in **Chapter 4**, our research has identified another crucial factor for the co-processing of BO at feeding temperatures. This factor is the critical temperature ( $T_{cr}$ ) at which a solid phase begins to form during the aging process, or fast aging. Previous studies have not reported any phase separation at temperatures lower than or equal to 50 °C. We found that the  $T_{cr}$  for BO fast aging is 80 °C. This means that the solid phase starts to form rapidly above this temperature. In summary, the findings of our research show that the aging process of BO is highly temperature-dependent, and the critical time for solid formation decreases with increasing temperature.

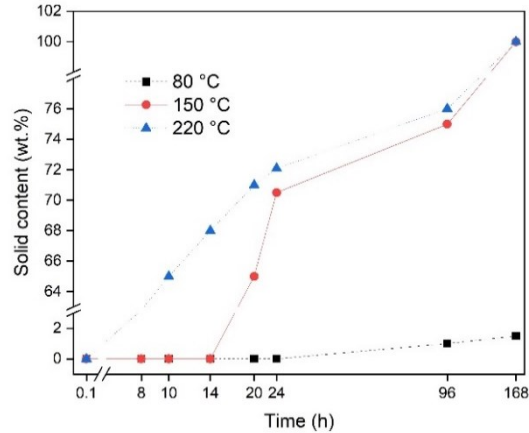


**Figure 5. 9.** Influence of temperature in solid content production in aging experiments.

## 5. 6 INFLUENCE OF METALLIC SPECIES IN BO AGING

Further characterization of the BO was conducted to investigate the correlation between immersion and aging experiments at co-FCC feeding temperatures. The aged BO used for comparison was obtained from the aging experiments carried out at a temperature of 150 °C for 24 hours, which allowed for the clear separation of the three distinct phases - film, top (liquid), and bottom (solid). Also, the immersion experiments were conducted for 24 hours. The immersion-BO used was the one previously used for the immersion of CS, described in **Chapter 4**. This metal was chosen due to its high susceptibility to corrosion under BO at this temperature. The purpose of comparing the immersion-BO with the aged BO was to investigate the effect of metal ions produced as a result of **Equation 4. 2** on BO aging and on its phase separation. The results showed that the immersion-BO, did not exhibit clear phase separation. Instead, the entire sample aged, resulting in a viscous and thick liquid with an even more viscous layer or sediment at the bottom.

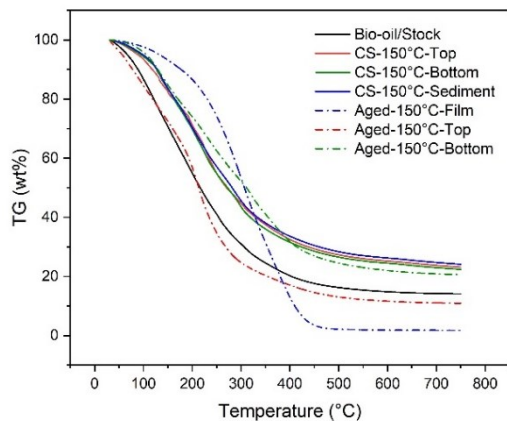


**Figure 5. 10.** Influence of immersed metal (CS) in BO aging.

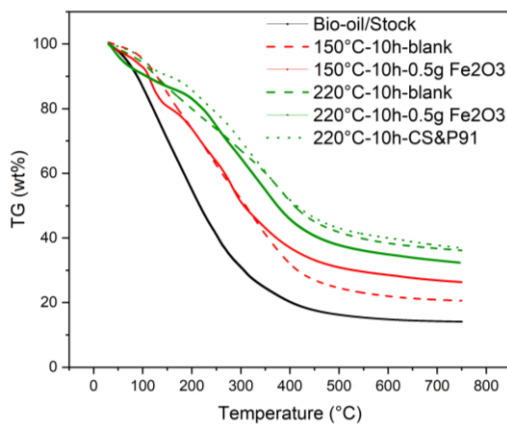


**Figure 5. 11.** Influence of immersed Fe-oxide in BO aging.

As illustrated in **Figure 5. 10**, the three layers observed in the immersion-BO were of the same nature as all three presented the same TG curves, which shifted upper-right in comparison to unaged BO. The TG profile of the bottom layer seen in the aging experiment was also similar to those of the immersion-BO. This indicates that the corrosion process of the highly susceptible metal, CS, did not promote phase separation but instead contributed to the aging of the entire BO

sample to the levels of the layer with the highest level of aging, which was the bottom layer when no immersed sample was present.

In **Chapter 4**, a set of experiments were carried out to determine the origin of the high pressure observed in immersion experiments involving BO. The aim was to distinguish whether the pressure increase was mainly attributed to the thermal decomposition of some of the BO constituents or originated from the anodic reaction described in **Equation 4. 2**, which generates H<sub>2</sub>. The findings of the experiments indicate that the anodic reaction is the principal source of pressure rise. As shown in **Figure 5. 11**, the addition of Fe<sub>2</sub>O<sub>3</sub> did not significantly alter the TG curve of the aged BO sample, which was employed as a blank test at both 150 and 220 °C. Similarly, the TG curve for the immersed-BO with CS and P91 did not vary considerably from the TG curve used as a blank test at 220 °C. All the curves exhibited a shift to the upper-right from the unaged BO, but did not promote phase separation. Therefore, it can be suggested that the presence of metal ions enhances the aging process in BO, but it is not associated with phase separation, as previously discussed.

# CHAPTER 6 CONCLUSIONS AND FUTURE WORK

In conclusion, the aim of this study was to examine the impact of FCC feeding temperatures on the corrosivity and thermal stability of BO. A series of experiments were designed and executed to assess the corrosion susceptibility of structural metals commonly used in the FCC unit and to investigate the influence of the thermal instability of BO on co-FCC feeding conditions. The findings of this research provide crucial risk assessment insights under those conditions. The remaining challenges outlined below can be addressed through further work, which will be instrumental in advancing the upgrading of BO through co-processing.

## 6.1 CONCLUSIONS

- The results of the study highlight the challenging conditions faced by FCC feeding lines when exposed to temperatures ranging from 80 to 220 °C in the presence of BO. The experiments conducted in this study demonstrate that CS, P91, and SS 304L are not suitable materials for these lines under these conditions. The immersion experiments at different temperatures revealed that corrosion rates of CS, P91, and SS 304L increased with temperature, reaching peak values of 51.96, 73.32, and 13.25 mm/y respectively at 220 °C. The addition of 9 wt.% Cr in P91 was not sufficient to resist BO at temperatures above 80 °C, nor was the higher amount of Cr, Mo, and Ni in SS 304L, which still showed significant corrosion at high temperatures. On the other hand, SS 316L had moderate corrosion rate of

1.77 mm/y at 220 °C. The estimated activation energy between 80 and 220 °C revealed that the corrosion of these four metals is influenced by the diffusion of passive species from the protective film. As a result, 80 °C was identified as the critical temperature at which active corrosion begins. HX performed exceptionally well, showing non-affected surfaces and near zero weight loss, although it is a more expensive alloy compared to the other four steels. The results provide valuable insights into the impact of temperature on the corrosivity of different structural steels in BO, providing a basis for selecting appropriate materials for FCC feeding lines. Based on the results, it is not recommended to inject BO into the co-FCC over 50 °C due to its high corrosivity.

- Accelerated aging experiments conducted in this study demonstrated that both exposure time and temperature contribute to aging reactions among reactive functional groups in BO. The study observed three layers of phase in the aged samples, including a film layer, a top liquid layer, and a bottom solid layer. The impact of temperature was found to be more severe than that of time, as TGA results showed that the solid phase (high-molecular-weight molecules) shifted more aggressively from unaged BO at higher temperatures than during longer exposure times. The solid content (film and solid) was found to increase exponentially with temperature, with values of 1 wt.%, 75 wt.%, and 76 wt.% at 80 °C, 150 °C, and 220 °C, respectively, after 24 hours of aging. These findings confirmed that 80 °C is also the critical temperature for fast aging of BO, and the solid content starts to increase from this temperature. Reactive functional groups in BO require less aging time for solid production (char, coke) at higher temperatures. It is not recommended to inject BO into co-FCC above the recommended temperature of 50 °C, as it could result in intense

phase separation and solids production, potentially leading to pipe plugging.

- Results from the correlation of data from objective 1 and objective 2 showed that at temperatures above 80 °C, the thermal instability of BO generates a non-homogeneous fluid. As a result, metal components in the FCC feeding lines are exposed to varying environments. The TGA results showed that the different phases obtained due to BO aging are composed of different organic matter, causing some phases to be more or less corrosive than the initial raw BO.

## **6.2 FUTURE WORK**

Based on the findings mentioned above, additional research is necessary to clarify the impact of phase separation on the corrosion of FCC construction materials, and to identify the most economical choice (MOC) for BO feeding lines. To accomplish this, the following steps are recommended:

- Conduct accelerated aging experiments on BO to promote phase separation.
- Collect a sufficient quantity of each phase from the aging experiments and perform immersion tests with various structural metals to evaluate the corrosivity of each phase.
- Develop a method to perform immersion tests with the solid phases obtained from the aging experiments.
- Conduct a cost-effectiveness analysis to determine the best approach, whether upgrading the metals in the FCC feeding lines or improving the BO through physical methods, to enhance its corrosivity, thermal stability, and miscibility.

## REFERENCES

- [1] J. A. Melero, J. Iglesias, and A. Garcia, “Biomass as renewable feedstock in standard refinery units. Feasibility, opportunities and challenges,” *Energy and Environmental Science*, vol. 5, no. 6. Royal Society of Chemistry, pp. 7393–7420, 2012. doi: 10.1039/c2ee21231e.
- [2] A. Demirbas, “Present and future transportation fuels,” *Energy Sources, Part A: Recovery, Utilization and Environmental Effects*, vol. 30, no. 16, pp. 1473–1483, Oct. 2008, doi: 10.1080/15567030701258519.
- [3] H. Wang, A. Gross, and J. Liu, “Influence of methanol addition on bio-oil thermal stability and corrosivity,” *Chemical Engineering Journal*, vol. 433, Apr. 2022, doi: 10.1016/j.cej.2021.133692.
- [4] F. T. R. Silalahi, T. M. Simatupang, and M. P. Siallagan, “Biodiesel produced from palm oil in Indonesia: Current status and opportunities,” *AIMS Energy*, vol. 8, no. 1. AIMS Press, pp. 81–101, 2020. doi: 10.3934/energy.2020.1.81.
- [5] D. Mohan, C. U. Pittman, and P. H. Steele, “Pyrolysis of wood/biomass for bio-oil: A critical review,” *Energy and Fuels*, vol. 20, no. 3. pp. 848–889, May 2006. doi: 10.1021/ef0502397.
- [6] S. Xiu and A. Shahbazi, “Bio-oil production and upgrading research: A review,” *Renewable and Sustainable Energy Reviews*, vol. 16, no. 7. pp. 4406–4414, Sep. 2012. doi: 10.1016/j.rser.2012.04.028.

- [7] S. O. Ilyin and V. v. Makarova, “Bio-Oil: Production, Modification, and Application,” *Chemistry and Technology of Fuels and Oils*, Mar. 2022, doi: 10.1007/s10553-022-01348-w.
- [8] X. Han, H. Wang, Y. Zeng, and J. Liu, “Advancing the application of bio-oils by co-processing with petroleum intermediates: A review,” *Energy Conversion and Management: X*, vol. 10, Jun. 2021, doi: 10.1016/j.ecmx.2020.100069.
- [9] A. R. K. Gollakota, N. Kishore, and S. Gu, “A review on hydrothermal liquefaction of biomass,” *Renewable and Sustainable Energy Reviews*, vol. 81. Elsevier Ltd, pp. 1378–1392, Jan. 01, 2018. doi: 10.1016/j.rser.2017.05.178.
- [10] R. M. Connatser, M. G. Frith, J. Jun, S. A. Lewis, M. P. Brady, and J. R. Keiser, “Approaches to investigate the role of chelation in the corrosivity of biomass-derived oils,” *Biomass Bioenergy*, vol. 133, Feb. 2020, doi: 10.1016/j.biombioe.2019.105446.
- [11] H. Yang, R. Yan, H. Chen, C. Zheng, D. H. Lee, and D. T. Liang, “In-depth investigation of biomass pyrolysis based on three major components: Hemicellulose, cellulose and lignin,” *Energy and Fuels*, vol. 20, no. 1, pp. 388–393, Jan. 2006, doi: 10.1021/ef0580117.
- [12] Y. Han *et al.*, “Hydrotreatment of pyrolysis bio-oil: A review,” *Fuel Processing Technology*, vol. 195. Elsevier B.V., Dec. 01, 2019. doi: 10.1016/j.fuproc.2019.106140.

- [13] C. Sheng and J. L. T. Azevedo, “Estimating the higher heating value of biomass fuels from basic analysis data,” *Biomass Bioenergy*, vol. 28, no. 5, pp. 499–507, May 2005, doi: 10.1016/j.biombioe.2004.11.008.
- [14] A. Oasmaa, D. C. Elliott, and J. Korhonen, “Acidity of biomass fast pyrolysis bio-oils,” *Energy and Fuels*, vol. 24, no. 12, pp. 6548–6554, Dec. 2010, doi: 10.1021/ef100935r.
- [15] J. Jun, M. G. Frith, R. M. Connatser, J. R. Keiser, M. P. Brady, and S. Lewis, “Corrosion of Ferrous Alloys by Organic Compounds in Simulated Bio-Oils.” NACE CORROSION/19, (Nashville, TN: NACE, 2019).
- [16] D. Chen, J. Zhou, Q. Zhang, and X. Zhu, “Evaluation methods and research progresses in bio-oil storage stability,” *Renewable and Sustainable Energy Reviews*, vol. 40. Elsevier Ltd, pp. 69–79, 2014. doi: 10.1016/j.rser.2014.07.159.
- [17] J. P. Diebold and S. Czernik, “Additives To Lower and Stabilize the Viscosity of Pyrolysis Oils during Storage,” *Energy and Fuels*, vol. 11, no. 5, pp. 1081–1091, Jun. 1997, doi: 10.1021/ef9700339.
- [18] D. C. Elliott, A. Oasmaa, F. Preto, D. Meier, and A. v. Bridgwater, “Results of the IEA round robin on viscosity and stability of fast pyrolysis bio-oils,” in *Energy and Fuels*, Jun. 2012, vol. 26, no. 6, pp. 3769–3776. doi: 10.1021/ef300384t.
- [19] A. Chaala, T. Ba, M. Garcia-Perez, and C. Roy, “Colloidal properties of bio-oils obtained by vacuum pyrolysis of softwood bark: Aging and thermal stability,” *Energy and Fuels*, vol. 18, no. 5, pp. 1535–1542, Sep. 2004, doi: 10.1021/ef030156v.

- [20] A. D. R. Pinho, M. B. B. de Almeida, F. L. Mendes, V. L. Ximenes, and L. C. Casavechia, “Co-processing raw bio-oil and gasoil in an FCC Unit,” *Fuel Processing Technology*, vol. 131, pp. 159–166, 2015, doi: 10.1016/j.fuproc.2014.11.008.
- [21] S. van Dyk, J. Su, J. D. Mcmillan, and J. (John) Saddler, “Potential synergies of drop-in biofuel production with further co-processing at oil refineries,” *Biofuels, Bioproducts and Biorefining*, vol. 13, no. 3. John Wiley and Sons Ltd, pp. 760–775, May 01, 2019. doi: 10.1002/bbb.1974.
- [22] P. L. Cruz, E. Montero, and J. Dufour, “Modelling of co-processing of HDO-oil with VGO in a FCC unit,” *Fuel*, vol. 196, pp. 362–370, 2017, doi: 10.1016/j.fuel.2017.01.112.
- [23] G. Fogassy, N. Thegarid, G. Toussaint, A. C. van Veen, Y. Schuurman, and C. Mirodatos, “Biomass derived feedstock co-processing with vacuum gas oil for second-generation fuel production in FCC units,” *Appl Catal B*, vol. 96, no. 3–4, pp. 476–485, Jun. 2010, doi: 10.1016/j.apcatb.2010.03.008.
- [24] A. Eschenbacher *et al.*, “Fluid catalytic co-processing of bio-oils with petroleum intermediates: Comparison of vapour phase low pressure hydrotreating and catalytic cracking as pretreatment,” *Fuel*, vol. 302, Oct. 2021, doi: 10.1016/j.fuel.2021.121198.
- [25] R.D. Kane, “Corrosion in Petroleum Refining and Petrochemical Operations,” in *Corrosion: Environments and Industries*, ASM International, 2018, pp. 967–1014. doi: 10.31399/asm.hb.v13c.a0004211.

- [26] J. Jun, M. G. Frith, R. M. Connatser, J. R. Keiser, M. P. Brady, and S. Lewis, “Corrosion Susceptibility of Cr-Mo Steels and Ferritic Stainless Steels in Biomass-Derived Pyrolysis Oil Constituents,” *Energy and Fuels*, vol. 34, no. 5, pp. 6220–6228, May 2020, doi: 10.1021/acs.energyfuels.9b04406.
- [27] R. Sadeghbeigi, *Fluid Catalytic Cracking Handbook*, 4<sup>th</sup> ed. (2020): p 215–230.
- [28] J. R. Keiser, M. P. Brady, J. K. Thomson, R. M. Connatser, S. A. Lewis, and D. N. Leonard, “Bio-Oil Properties and Effects on Containment Materials.” NACE CORROSION/14, (San Antonio, TX: NACE, 2014).
- [29] J. R. Keiser *et al.*, “Corrosion and Chemical Characterization of Bio-Oils from Biomass with Varying Ash and Moisture Contents.” NACE CORROSION/21, (Salt Lake City, UT: NACE, 2021).
- [30] B. A. Mei, O. Munteshari, J. Lau, B. Dunn, and L. Pilon, “Physical Interpretations of Nyquist Plots for EDLC Electrodes and Devices,” *Journal of Physical Chemistry C*, vol. 122, no. 1, pp. 194–206, Jan. 2018, doi: 10.1021/acs.jpcc.7b10582.
- [31] J. Jun, D. Sulejmanovic, J. R. Keiser, M. P. Brady, and M. D. Kass, “Evaluation of Corrosion Susceptibility of Structural Steels in Biomass Derived Pyrolysis Oil,” NACE CORROSION/21, (Salt Lake City, UT: NACE, 2021).
- [32] J. Jun, D. Sulejmanovic, J. R. Keiser, M. P. Brady, and M. D. Kass, “Corrosion Behavior of Alloy Structural Steels in Catechol and Biomass-Derived Pyrolysis Oils,” NACE CORROSION/21, (Salt Lake City, UT: NACE, 2021).

- [33] M. P. Brady, J. R. Keiser, D. N. Leonard, A. H. Zacher, K. J. Bryden, and G. D. Weatherbee, "Corrosion of stainless steels in the riser during co-processing of bio-oils in a fluid catalytic cracking pilot plant," *Fuel Processing Technology*, vol. 159, pp. 187–199, 2017, doi: 10.1016/j.fuproc.2017.01.041.
- [34] Z. Yang, A. Kumar, and R. L. Huhnke, "Review of recent developments to improve storage and transportation stability of bio-oil," *Renewable and Sustainable Energy Reviews*, vol. 50. Elsevier Ltd, pp. 859–870, Jun. 04, 2015. doi: 10.1016/j.rser.2015.05.025.
- [35] N. Bruun, J. Lehmusto, F. Tesfaye, J. Hemming, and L. Hupa, "Amino Acids Reduce Mild Steel Corrosion in Used Cooking Oils," *Sustainability (Switzerland)*, vol. 14, no. 7, Apr. 2022, doi: 10.3390/su14073858.
- [36] N. S. Nasri, M. M. Ahmed, M. Amruddin, U. D. Hamza, J. Mohammed, and Z. H. Mohd, "Corrosion Inhibition Study of Upgraded Bio-Oil Derived Empty Fruit Bunch Using Alumina," *Applied Mechanics and Materials*, vol. 695, pp. 114–117, Nov. 2014, doi: 10.4028/www.scientific.net/amm.695.114.
- [37] M. A. Raza, N. Z. Al-Mutairi, Al-Rabiah, Al-Sulaiman, and Al-Muhtaseb, "Inhibition of steel corrosion in biofuels by alcohols and glycols: A review," *Journal of Molecular Liquids*, vol. 211, pp. 939–950, 2015.
- [38] D. Bhattacharjee, and A. K. Agarwal, "Effect of 2-ethylhexanol addition on diesel and biodiesel blend properties and corrosion," *Fuel*, vol. 89, no. 12, pp. 3868–3873, 2010.

- [39] ASTM G31 (latest revision), “Standard Guide for Laboratory Immersion Corrosion Testing of Metals” (ASTM), doi: 10.1520/G0031-12A.
- [40] J. Liu, A. Alfantazi, and E. Asselin, “High temperature corrosion of titanium under conditions relevant to pressure leaching: Mass loss and electrochemistry,” *Corrosion*, vol. 71, no. 3, pp. 352–366, Mar. 2015, doi: 10.5006/1366.
- [41] R. N. Traxler, J. W. Romberg, and H. E. Schweyer, “Rotary Viscometer for Determination of High Consistencies,” *Industrial and Engineering Chemistry*, vol. 14, no. 4, pp. 340–344, Apr. 1942.
- [42] D. H. Fitzgerald Ltd, “Technical Assessment of the Anton Paar DMA5000 density meter,” Jan. 2000.
- [43] P. Bruttel and R. Schlink, “Water Determination by Karl Fischer Titration,” Feb. 2006.
- [44] “Maintenance Manual for Laboratory Equipment,” Chapter 3, pH Meter.
- [45] S. Hosokai, K. Matsuoka, K. Kuramoto, and Y. Suzuki, “Modification of Dulong’s formula to estimate heating value of gas, liquid and solid fuels,” *Fuel Processing Technology*, vol. 152, pp. 399–405, Nov. 2016, doi: 10.1016/j.fuproc.2016.06.040.
- [46] M. W. Davidson and M. Abramowitz, “Optical Microscopy.”
- [47] W. D. Callister and D. G. Rethwisch, “Materials Science and Engineering: An Introduction,” John Wiley & Sons, 2020.
- [48] C. Pandey, A. Giri, and M. M. Mahapatra, “Evolution of phases in P91 steel in various heat treatment conditions and their effect on microstructure stability and

- mechanical properties,” *Materials Science and Engineering A*, vol. 664, pp. 58–74, May 2016, doi: 10.1016/j.msea.2016.03.132.
- [49] C. Pandey, M. M. Mahapatra, P. Kumar, R. S. Vidyathy, and A. Srivastava, “Microstructure-based assessment of creep rupture behaviour of cast-forged P91 steel,” *Materials Science and Engineering A*, vol. 695, pp. 291–301, May 2017, doi: 10.1016/j.msea.2017.04.037.
- [50] C. Pandey, A. Giri, M. M. Mahapatra, and P. Kumar, “Characterization of microstructure of HAZs in as-welded and service condition of P91 pipe weldments,” *Metals and Materials International*, vol. 23, no. 1, pp. 148–162, Jan. 2017, doi: 10.1007/s12540-017-6394-5.
- [51] M. Liu, Y. Zeng, and J. L. Luo, “Influence of Major Operating Parameters (Temperature, Pressure, and Flow Rate) on the Corrosion of Candidate Alloys for the Construction of Hydrothermal Liquefaction Biorefining Reactors,” *Energy and Fuels*, vol. 36, no. 6, pp. 3134–3153, Mar. 2022, doi: 10.1021/acs.energyfuels.1c04046.
- [52] D. Kong *et al.*, “Anisotropic response in mechanical and corrosion properties of hastelloy X fabricated by selective laser melting,” *Constr Build Mater*, vol. 221, pp. 720–729, Oct. 2019, doi: 10.1016/j.conbuildmat.2019.06.132.
- [53] K. D. Vernon-Parry, “Scanning Electron Microscopy: an introduction.” *III-Vs Review*, Vol. 13, no. 4, 2000.
- [54] H. Stanjek and W. Häusler, “Basics of X-ray Diffraction,” *Hyperfine Interactions*, Vol. 154, pp. 107–119, 2004.

- [55] H. E. Townsend, “Effects of Alloying Elements on the Corrosion of Steel in Industrial Atmospheres,” *Corrosion*, Vol. 57, no. 6, Jun. 2001.
- [56] NACE International., *Standard recommended practice : preparation, installation, analysis, and interpretation of corrosion coupons in oilfield operations*. NACE International, 1999.
- [57] S. A. Bradford, *Corrosion control*. CASTI Pub., 2001.
- [58] K. Li, Y. Zeng, and J. L. Luo, “Condensed phase corrosion of P91 and DSS 2205 steels at advanced oxygen-fired pressurized fluidized bed combustion plants,” *Materials and Corrosion*, vol. 72, no. 4, pp. 757–771, Apr. 2021, doi: 10.1002/maco.202011882.
- [59] R. Sánchez-Tovar, M. T. Montañés, J. García-Antón, and A. Guenbour, “Influence of temperature and hydrodynamic conditions on the corrosion behavior of AISI 316L stainless steel in pure and polluted H<sub>2</sub>O: Application of the response surface methodology,” *Mater Chem Phys*, vol. 133, no. 1, pp. 289–298, Mar. 2012, doi: 10.1016/j.matchemphys.2012.01.024.
- [60] S. Takasaki and Y. Yamada, “Effects of temperature and aggressive anions on corrosion of carbon steel in potable water,” *Corros Sci*, vol. 49, no. 1, pp. 240–247, Jan. 2007, doi: 10.1016/j.corsci.2006.05.035.
- [61] K. v. Akpanyung and R. T. Loto, “Pitting corrosion evaluation: A review,” in *Journal of Physics: Conference Series*, Dec. 2019, vol. 1378, no. 2. doi: 10.1088/1742-6596/1378/2/022088.

- [62] D. A. Skobir and M. Spiegel, "The stability of cast alloys and cvd coatings in a simulated biomass-combustion atmosphere," *Materiali in tehnologije*, Vol. 40, no. 6, p 247, 2006.
- [63] C. P. O'Hagan, R. A. Barrett, S. B. Leen, and R. F. D. Monaghan, "Effect of high-temperature corrosion on the service life of P91 piping in biomass co-firing," *Journal of Pressure Vessel Technology, Transactions of the ASME*, vol. 138, no. 2, Apr. 2016, doi: 10.1115/1.4032648.
- [64] S. Paul and M. D. F. Harvey, "Corrosion testing of Ni alloy HVOF coatings in high temperature environments for biomass applications," in *Journal of Thermal Spray Technology*, Mar. 2013, vol. 22, no. 2–3, pp. 316–327. doi: 10.1007/s11666-012-9820-8.
- [65] H. Wang and J. Liu, "Emulsification and corrosivity study of bio-oil and vacuum gas oil mixtures with a novel surfactant system," *Fuel*, vol. 333, Feb. 2023, doi: 10.1016/j.fuel.2022.126460.
- [66] C. Schroer, O. Wedemeyer, J. Novotny, A. Skrypnik, and J. Konys, "Selective leaching of nickel and chromium from Type 316 austenitic steel in oxygen-containing lead-bismuth eutectic (LBE)," *Corros Sci*, vol. 84, pp. 113–124, 2014, doi: 10.1016/j.corsci.2014.03.016.
- [67] Z. Ahmad, *Principles of Corrosion Engineering and Corrosion Control*, 1<sup>st</sup> ed. 2006.
- [68] H. Darmstadt, M. Garcia-Perez, A. Adnot, A. Chaala, D. Kretschmer, and C. Roy, "Corrosion of metals by bio-oil obtained by vacuum pyrolysis of softwood bark residues. An X-ray photoelectron spectroscopy and Auger electron spectroscopy

study,” *Energy and Fuels*, vol. 18, no. 5, pp. 1291–1301, Sep. 2004, doi: 10.1021/ef0340920.

- [69] W. Zhang, Z. Zhao, A. Zheng, S. Chang, and H. Li, “Characterization and storage stability analysis of bio-oil,” *Journal of Fuel Chemistry and Technology*, Vol. 40, no. 2, pp. 184–189, 2012.

# **APPENDIX A – CHEMICAL COMPOSITIONS**

This section includes the chemical compositions of structural steels previously tested through immersion and EIS experiments by various authors.

## **A.1 CHEMICAL COMPOSITIONS OF STRUCTURAL STEELS**

## A.1 CHEMICAL COMPOSITIONS OF STRUCTURAL STEELS

**Table A.1. 1.** Chemical compositions of commonly used structural steels in co-processing applications testes in previous studies.

Alloy	Fe	C	Cr	Cu	Mn	Mo	Ni	P	Si	S	Refs
<b>CS A36</b>	Bal.	0.20	0.05	0.04	0.74	0.01	0.01	0.01	0.01	0.01	[3]
<b>CS 1018</b>	Bal.	0.15	-	-	0.60	-	-	-	-	-	[29]
<b>CS H44</b>	Bal.	0.11	-	-	1.00	-	-	0.03	0.21	0.02	[35]
<b>2.25Cr-1Mo</b>	Bal.	0.10	2.25	-	0.40	1.00	-	-	0.20	-	[29]
<b>2.25Cr-1Mo</b>	Bal.	0.09	2.22	0.09	0.51	1.01	0.14	-	0.17	-	[31]
<b>5Cr-1Mo</b>	Bal.	-	5.00	-	-	1.00	-	-	-	-	[32]
<b>9Cr-1Mo</b>	Bal.	0.07	9.08	0.03	0.56	0.99	0.09	-	0.61	-	[32]
<b>SS 201</b>	Bal.	0.08	15.9	0.71	6.97	0.27	4.46	-	0.48	-	[33]
<b>SS 304L</b>	Bal.	0.02	18.3	-	1.70	-	9.00	-	0.50	-	[29]
<b>SS 316L</b>	Bal.	0.02	16.4	-	1.60	2.10	10.2	-	-	-	[28]
<b>SS 317L</b>	Bal.	0.02	17.7	0.11	1.69	2.97	14.2	-	0.56	-	[33]
<b>SS 409</b>	Bal.	0.02	11.0	-	0.30	-	-	-	0.40	-	[29]
<b>SS 410</b>	Bal.	0.01	12.1	0.12	0.13	0.03	0.15	-	0.49	-	[33]
<b>SS 430</b>	Bal.	0.04	16.9	0.13	0.26	0.05	0.15	-	0.33	-	[31]
<b>SS 430F</b>	Bal.	0.03	17.5	0.17	0.43	0.33	0.30	-	0.32	0.33	[31]